Geophysical Journal International

Geophys. J. Int. (2024) **239,** 841–861
Advance Access publication 2024 August 21
GJI Geomagnetism and Electromagnetism

https://doi.org/10.1093/gji/ggae297

Reliability of the palaeomagnetic signal recorded in a lava flow erupted on 4 December 2021 in La Palma (Canary Islands, Spain)

Manuel Calvo-Rathert,[1] Eva Vernet,[1] Josep M. Parés,[2] Vicente Soler,[3] Elisa-María Sánchez-Moreno,[1] María-Felicidad Bógalo,[1] Ángel Carrancho,[4] Yuhji Yamamoto[5] and Lidia Rodríguez-Méndez[6]

[1]*Departamento de Física, EPS, Universidad de Burgos, Av. Cantabria, s/n,* 09006 *Burgos, Spain. E-mail: mcalvo@ubu.es*
[2]*Geochronology & Geology, CENIEH, Paseo Sierra de Atapuerca 3,* 09002 *Burgos, Spain*
[3]*Instituto de Productos Naturales y Agrobiología (IPNA), Av. Astrofísico Francisco Sánchez, 3,* 38206 *San Cristóbal de La Laguna, Spain*
[4]*Área de Prehistoria. Departamento de Historia, Geografía y Comunicación, Universidad de Burgos,* 09001 *Burgos, Spain*
[5]*Marine Core Research Institute, Kochi University,* 783-8502 *Kochi, Japan*
[6]*Departamento de Geología, Universidad del País Vasco / Euskal Herriko Unibertsitatea,* 48080 *Bilbao, Spain*

Accepted 2024 July 30. Received 2024 July 22; in original form 2024 February 22

SUMMARY

A basaltic lava flow erupted from the Tajogaite volcano on 4 December 2021, in La Palma (Canary Islands, Spain) was sampled to find out to what extent reliable and correct information on both intensity and direction of the Earth's magnetic field can be obtained from the palaeomagnetic signal recorded in a lava flow which erupted under known conditions. Samples were taken every few centimetres across a flow up to a total of 27 oriented cores. Palaeomagnetic experiments showed a strong viscous overprint in many samples. Nevertheless, the mean palaeomagnetic direction obtained agrees well with the actual value from IGRF-13. Rock magnetic experiments were performed to obtain additional information about the quality and reliability of the results and the reasons for unsuccessful determinations. Analysis of mostly irreversible thermomagnetic curves showed that the carriers of remanence were magnetite and titanomagnetite of low and/or intermediate Curie-temperature. Hysteresis parameter ratios showed a pronounced variability across the flow. Analyses of frequency dependent susceptibility, IRM acquisition coercivity spectra and FORCs showed a noticeably presence of very low coercivity grains (multidomain and superparamagnetic-single domain boundary). Multimethod palaeointensity experiments were performed with the Thellier-Coe, multispecimen and Tsunakawa-Shaw methods. Only three of 25 cores from the flow yielded successful Thellier-Coe determinations, in agreement with the expected field value of 38.7 μT (IGRF-13). However, palaeointensities of 60 per cent of the specimens agree with the expected value performing an informal analysis without considering criteria thresholds. Four of six Tsunakawa-Shaw determinations performed on samples from the flow yielded correct results, but three multispecimen determinations providing apparently successful determinations largely underestimate the expected field intensity. Combination of three Thellier-Coe and four Tsunakawa-Shaw successful determinations yields a multimethod palaeointensity result $B = (36.9 \pm 2.0)$ μT in good agreement with the expected field intensity.

Key words: Palaeointensity; Rock and mineral magnetism; Palaeomagnetism; Oceanic hotspots and intraplate volcanism.

1. INTRODUCTION

The direction and intensity of palaeomagnetic records supply information about the past characteristics and variations of the Earth's magnetic field (EMF), supplying constraints necessary to understand processes occurring in the deep interior of the Earth (e.g. Biggin & Paterson 2014). Lava flows can be an important means to retrieve information related to such processes, as during their eruption and emplacement they acquire a thermoremanent magnetization (TRM) whose direction is in principle parallel or nearly parallel to the magnetizing field, while its intensity is proportional to the magnetizing field strength. Thus, directions of

the ancient EMF can be directly read from the palaeomagnetic record.

However, past intensities of the EMF—so called palaeointensities—cannot be directly determined from the remanence recorded in rocks. The intensity of remanent magnetization will depend on the intensity of the magnetizing field, but also on the magnetic properties of the carriers of remanence. Therefore, absolute palaeointensity determination experiments require the comparison of the natural remanence (NRM) recorded in the rocks with a laboratory acquired TRM in a known laboratory field B_{lab}. Thellier-type methods (Thellier & Thellier 1959) are regarded the most trustworthy, because they rely on a robust physical basis (Néel 1949), but successful determinations require TRM to be carried by non-interacting single-domain (SD) grains (e.g. Dunlop 2011, and references therein), a condition normally not rigorously met by natural rocks. Moreover, it is necessary that during palaeointensity determination experiments, no chemical, mineralogical or physical alteration affect the carriers of remanence. Thus, failure rates of Thellier-type palaeointensity determinations can be rather large and, even worse, in some cases, apparently reliable determinations may produce erroneous palaeointensity results (e.g. Calvo *et al.* 2002; Shcherbakov *et al.* 2019).

Several alternative methods have been proposed to avoid, or at least lessen chemical and/or mineralogical alterations, as well as the effect of multidomain (MD) grains. One of these methods is the multispecimen (MS) method (Dekkers & Böhnel 2006), which is based on a theoretical model proposed by Biggin & Poidras (2006) and is supposed to preclude incorrect palaeointensity determinations due to domain structure. Fabian & Leonhardt (2010), however, questioned the method because of the possibility systematic palaeointensity overestimates due to multidomain (MD) grains, which have been reported by Michalk *et al.* (2008, 2010) and Calvo-Rathert *et al.* (2016). A new MS measurement protocol including extra correction steps was proposed by Fabian & Leonhardt (2010) to prevent these overestimates.

A different kind of palaeointensity determination method was proposed by Shaw (1974). It uses alternating field (AF) demagnetization of NRM and TRM to allow determination of the NRM/TRM ratio as a function of coercivity, and a variety of modifications have been proposed to this approach. The Tsunakawa-Shaw method (Tsunakawa *et al.* 1997; Yamamoto *et al.* 2003), formerly called the LTD-DHT Shaw method, uses individual ARM corrections (Rolph & Shaw 1985), a double heating test (Tsunakawa & Shaw 1994) and low temperature demagnetization (LTD). A detailed description of the method is given by Yamamoto & Tsunakawa (2005). Some possible advantages of this approach include the measurement of single-domain (SD)-like remanences because LTD can erase MD-like components and the fact that the laboratory TRM acquisition process is thought to be analogous to a natural process, because samples are directly heated above the Curie temperature and cooled down in a field to room temperature.

The concurrent use of palaeointensity determination methods based on different principles can be a convenient approach to increase the reliability of the results obtained if coincidences are observed (e.g. de Groot *et al.* 2013, 2015; Monster *et al.* 2015a; Calvo-Rathert *et al.* 2019, 2022; Allington *et al.* 2021; García-Redondo *et al.* 2021; Sánchez-Moreno *et al.* 2021). The main objective of this study was to find out to what extent reliable and correct information on both intensity and direction of the EMF can be obtained from the palaeomagnetic signal recorded in a lava flow which erupted under known conditions (field value and eruption date and duration are known) using different palaeointensity determination methods. Rock-magnetic analyses have also been included in the study to obtain additional information about the quality and reliability of the results and the reasons for unsuccessful determinations.

Various palaeointensity investigations based on different determination methods have been already conducted on recent lava samples erupted in known geomagnetic field conditions to test the viability of methods and materials as means of obtaining an accurate record of EMF intensity (e.g. Böhnel *et al.* 2011; Calvo *et al.* 2002; Cromwell *et al.* 2015; Jeong *et al.* 2021; Fukuma 2023; Grappone *et al.* 2019; Tsunakawa & Shaw 1994; Valet *et al.* 2010). With this aim in mind, we sampled a basaltic lava flow erupted from the Tajogaite volcano on 4 December 2021, in the island of La Palma (Canary Islands). A preliminary rock-magnetic study carried out on earlier ejected material (unoriented lava flow and lapilli samples) from the 2021 eruption series in La Palma has recently been published by Parés *et al.* (2022).

2. GEOLOGICAL SETTING AND SAMPLING

La Palma forms part of the Canary Islands, an archipelago on the African Plate located some 100–500 km west of the Sahara continental margin on the eastern Atlantic Ocean (Fig. 1). It forms a roughly E–W oriented chain on the African plate, consisting of seven volcanic islands thought to have formed above a mantle plume as the plate moved east-northeastwards over a hotspot (e.g. Carracedo *et al.* 1998), with the oldest subaerial volcanism in Fuerteventura and the youngest in the westernmost islands of La Palma and El Hierro.

A detailed description of the geological evolution of La Palma including a large number of radiometric age data is given by Carracedo *et al.* (2001). Traditionally, La Palma has been divided into three main units (Klügel *et al.* 2017, and references therein): (i) the basal complex (3–4 Ma) which includes an uplifted and tilted Pliocene seamount sequence and a plutonic complex, an older volcanic series (2–0.7 Ma) which comprises the Taburiente shield volcano, and the recent Cumbre Vieja series (0.7 Ma to present). The Cumbre Vieja series is a N–S, 25 km long ridge that makes up the southern half of the island, and it is thought to be an active rift zone.

The Tajogaite eruption was the longest and most voluminous eruption in La Palma in historical times (e.g. González 2022) with more than 200 million m^3 ejected on the western foothills of the volcano. Volcanic activity lasted a total of 85 days, between 19 September and 13 December 2021. The lavas erupted at La Palma are mainly tephrites to basanites that are compositionally similar to those from other historical eruptions in La Palma (Carracedo *et al.* 2022). They are porphyritic, variably vesiculated and with a phenocryst content of subhedral and compositionally zoned clinopyroxene as the main mineral phase with lesser amounts of olivine crystals in early erupted lavas (Carracedo *et al.* 2022), and were emitted as a'a and pahoehoe lava types (e.g. Palanco *et al.* 2022). Lava flows descended towards the coast and reached the ocean at two spots, forming two lava deltas (Alonso *et al.* 2023).

The lava flows also cut communications in the southwestern flank of the island, and only in September 2022 the construction of a new road in the lava field could be started. The construction of the new road allowed us to access and sample a newly open and therefore fresh rock surface of the flow emplaced on 4 December 2021 (Fig. 2). On 14 September 2022, we carried out a sampling across the whole flow. The flow had a thickness of approximately 2.2 m, and we took 27 cores using a portable gasoline powered

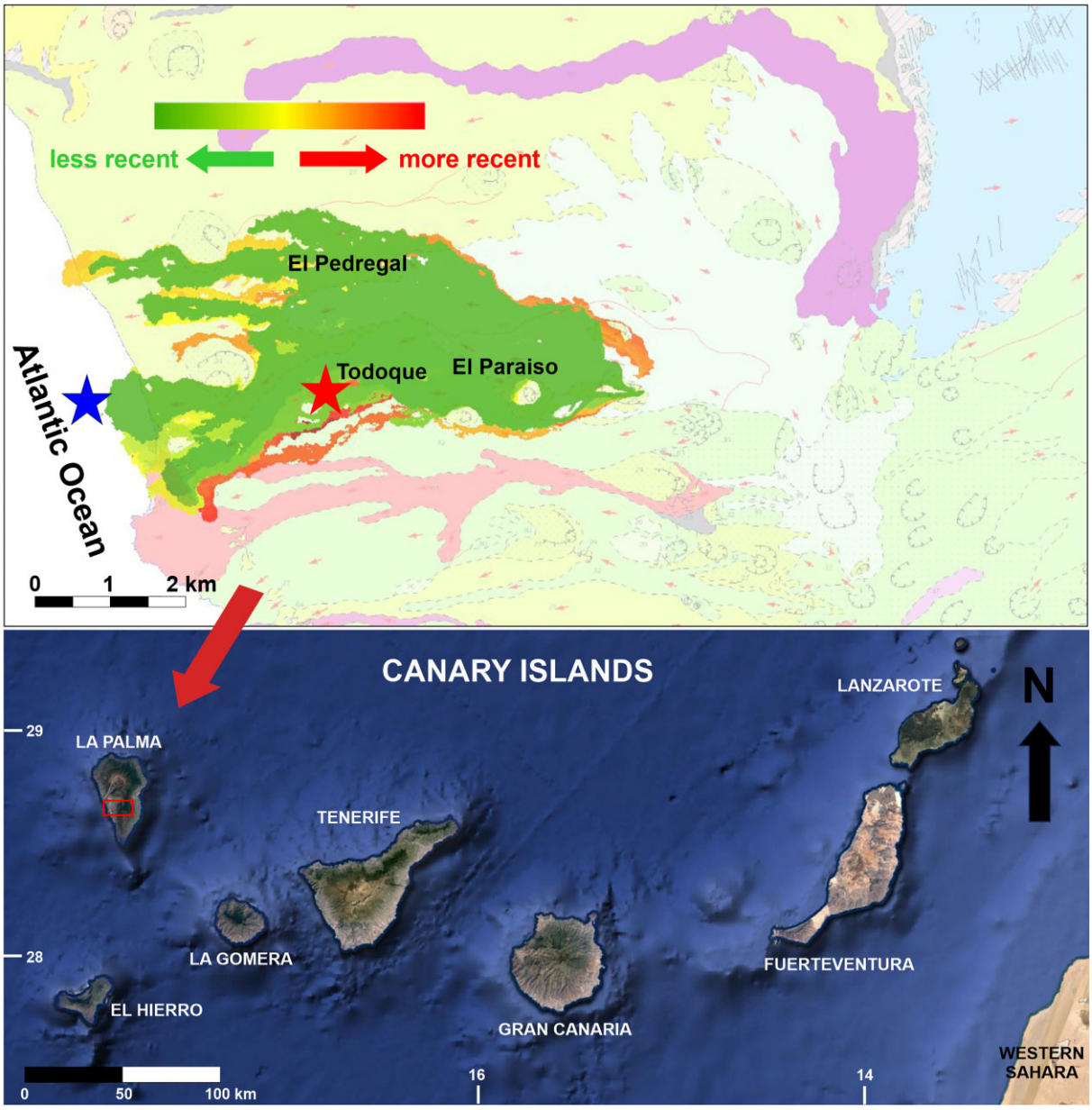

Figure 1. Location of the sampled lava flow in the island of la Palma. Lower map: Canary Islands map (adapted from Google Earth). A red rectangle on the island of La Palma shows the position of the inset on the left. Upper map: Lava flows generated by the eruptions la Palma between 19 September and 13 December 2021 (a colour code varying between green and red shows the timing of the eruptions. A red star indicates sampling site location in the flow (28.609°N; 17.900°W), a blue one the location of the submarine lava samples. Adapted from INFOIGME (2024).

drill (Fig. 2). Thus, on average, a sample was obtained every 5–10 cm, although sampling was somewhat tighter at the upper and lower ends. Cores were oriented with a Pomeroy orientation device equipped with both magnetic and solar compass.

In addition, we also obtained unoriented specimens from a lava flow cooled down in the ocean in a lava delta and correspond to a lava emitted before the December 4 flow. Specimens stem from the outer crust (sample TV-832, cooled very rapidly) and the massive interior of a pillow-lava (sample TV-833) taken with an unmanned underwater vehicle directed from a ship from the Spanish Institute of Oceanography (IEO-CSIC). All samples were transported by plane and stored in the palaeomagnetic laboratory of the University of Burgos.

3. PALAEOMAGNETIC MEASUREMENTS

Palaeomagnetic measurements were conducted in the University of Burgos (Spain) with a 2G cryogenic magnetometer. Thermal demagnetization was started only one month after collecting the samples. It was performed with a TD48-DC (ASC) furnace on one specimen from each of the 27 cores sampled across the flow. AF-demagnetization was started on March 2023, six months after sample collection. It was carried out on specimens from 19 cores of the flow with an LDA-3 (Agico) tumbling AF demagnetizer. The Remasoft 3.0 software (Chadima & Hrouda 2006) was used for the analysis of demagnetization data.

Figure 2. Sampled lava flow. Sampled lava flow with the position and number of the sampled cores.

Table 1 displays palaeomagnetic results obtained with both techniques. Demagnetization plots across the whole flow show a rather differing appearance (Fig. 3). In few cases, rather simple plots with one palaeomagnetic component and a moderate or weak viscous overprint are observed. This kind of palaeomagnetic behaviour appears mainly at the upper and lower ends of the flow, but also in some cores sampled in its central part (Figs 3a and b). In most cases, however, the characteristic palaeomagnetic component is associated with a strong viscous overprint (Figs 3c and d), an unexpected observation in this very young flow. Nevertheless, determination of palaeomagnetic directions was straightforward and results obtained agree well with expected IGRF-13 (Alken *et al.* 2021) values. Characteristic remanence directions were in most cases obtained from a large number of demagnetization steps (a mean value of $N = 12$ steps for thermal and $N = 9$ steps for AF demagnetization) yielding generally low MAD values (a mean MAD = 5.0 for thermal and MAD = 3.6 for AF demagnetization). Only two samples (CVC2-3 in the upper part of the flow and CVC2-22 from the lower part) yielded anomalous palaeomagnetic directions, probably related to components with overlapping coercivity or unblocking temperature spectra and were not included in the calculations of palaeomagnetic mean directions. Table 1 and Fig. S1 show mean palaeomagnetic directions calculated from thermally and AF demagnetized specimens as well as from all samples, the latter combining thermal and AF-demagnetization results obtained from specimens from the same core. Mean directions calculated from only thermally or only AF-demagnetized specimens as well as from all data agree well with the direction provided by the IGRF-13 (Alken *et al.* 2021, Fig. S1).

Table 1. Palaeomagnetic results.

SAMPLE	TH				AF				MEAN		β
	DEC	INC	N	MAD	DEC	INC	N	MAD	DEC	INC	
CVC2-1	333.1	39.3	12	6.9	358.2	28.7	9	1.0	333.1	39.3	23.2
CVC2-2	336.3	57.2	15	3.9					336.3	57.2	
CVC2-3*	2.0	-13.5	4	7.8	32.6	−18.2	10	3.4	17.1	−16.4	29.8
CVC2-4	4.9	44.8	15	4.8					4.9	44.8	
CVC2-5	7.4	48.2	5	3.4	346.5	36.4	10	3.4	356.0	42.8	19.3
CVC2-6	34.5	41.7	9	3.4					34.5	41.7	
CVC2-7	1.3	46.1	13	6.3	353.9	36.3	11	2.8	357.3	41.3	11.3
CVC2-8	354.9	28.0	11	6.5	358.5	40.2	9	3.7	356.6	34.1	12.6
CVC2-9	343.9	46.6	16	8.5	348.1	48.1	7	4.4	346.0	47.4	3.2
CVC2-10	22.7	31.7	14	4.9	348.9	43.6	9	6.0	7.2	38.9	29.0
CVC2-11	6.1	37.9	16	3.0	357.8	44.5	10	3.5	2.2	41.3	9.1
CVC2-12	349.6	49.7	15	11.0	351.2	42.7	9	3.1	350.5	46.2	7.1
CVC2-13	5.2	40.3	13	2.3					5.2	40.3	
CVC2-14	10.4	51.9	13	5.3	349.6	50.0	10	3.7	359.8	51.4	13.2
CVC2-15	346.8	15.5	8	5.7	353.0	33.8	7	4.5	349.7	24.7	19.1
CVC2-16	350.9	40.7	4	4.7	355.0	33.2	9	1.5	353.1	37.0	8.2
CVC2-17	0.8	40.1	16	4.4					0.8	40.1	
CVC2-18	353.5	32.2	14	5.7	5.8	32.7	9	4.8	359.6	32.6	10.4
CVC2-19	359.3	31.1	15	3.8					359.3	31.1	
CVC2-20	358.8	43.1	13	4.6	338.9	32.3			348.1	38.1	19.1
CVC2-21	341.7	48.0	15	9.8	349.8	40.2	4	3.7	346.0	44.2	9.7
CVC2-22*	258.7	-50.9	5	1.9	255.3	-43.2	7	2.7	256.9	-47.1	8.0
CVC2-23	355.9	26.1	15	5.5					355.9	26.1	
CVC2-24	349.3	29.7	13	2.9	354.3	47.1	9	5.2	351.5	38.4	17.8
CVC2-25	10.9	34.4	8	1.9					10.9	34.4	
CVC2-26	358.7	37.7	6	2.7	354.4	37.0	9	2.8	356.5	37.4	3.5
CVC2-27	352.3	38.5	9	4.0	359.0	36.4	10	1.8	353.1	37.0	5.7

	N	DEC	INC	k	α_{95}	Δ
MEAN-TH	25	358.1	40.0	34.5	5.0	3.7
MEAN-AF	17	353.2	39.2	106.4	3.5	2.9
MEAN	25	357.2	39.8	55.2	3.9	3.2
IGRF 2020		355.5	37.0			

SAMPLE: core number; DEC and INC: declination and inclination of ChRM for thermally demagnetized specimens (TH), AF demagnetized specimens (AF) and mean value obtained for each core (MEAN). *N*: number of demagnetization steps used to determine directions (additionally, the origin has been included); MAD: maximum angular deviation for each determination; β: angle between thermally and AF demagnetized specimens from the same core. MEAN-TH and MEAN-AF: mean declination (DEC) and inclination (INC) values for thermally and AF demagnetized specimens for the whole flow; MEAN: mean declination (DEC) and inclination (INC) values for the whole flow (an asterisk identifies two samples with anomalous directions excluded from the mean); IGRF-13: declination (DEC) and inclination (INC) of the magnetic field at the lava flow location on 4 December 2021, obtained from IGRF-13 (Alken *et al.* 2021). *N*: number of specimens/samples used for flow mean calculation; α_{95}: radius of 95 per cent confidence cone. *k*: precision parameter. Δ: angle between mean flow directions and the field direction obtained from IGRF-13.

In addition to these palaeomagnetic measurements performed on the December 4th flow, two unoriented specimens belonging to the ocean-cooled lava flow were subjected to AF-demagnetization with the aim of analysing the magnetic properties of this material regarding its ability to provide a reliable intensity signal of the EMF. One of the specimens belonged to the outer crust of the flow and, together with its characteristic remanent magnetization (ChRM) it showed the presence of a very strong viscous component, which was easily erased at 4 mT. The other sample belonged to the massive interior of the flow and although it also displayed a viscous secondary component, this was much weaker.

Magnetic viscosity indices (Thellier & Thellier 1944; Prévot 1981) were determined for most samples of the flow. As not enough untreated specimens were available, only AF-demagnetized ones were used. Samples were stored for two weeks in ambient magnetic field such that the field was parallel to the cylindrical axis of each specimen, and subsequently their remanence was measured ($\vec{M}_N$). Then, samples were stored again for two weeks in ambient field, but antiparallel to the initial position, and their remanence was measured again ($\vec{M}_R$). Originally, the viscosity index v is determined by the ratio $v = \frac{|\vec{M}_N - \vec{M}_R|}{|\vec{M}_N + \vec{M}_R|}$, that is the viscous remanence VRM acquired in two opposite directions for one month is normalized to stable remanence. However, as the remaining remanence of AF demagnetized specimens is very weak, this produces artificially enhanced viscosity indices. For this reason, in the present study viscosity indices v have been calculated by normalizing VRM to the NRM before demagnetization, with $v = \frac{|\vec{M}_N - \vec{M}_R|}{2\ \mathrm{NRM}}$. Viscosity indices calculated this way yield relatively moderate values, with a $v = (2.6 \pm 1.7)$ per cent. These indices are probably lower than the values which would have been obtained with the standard calculation method. It should be however noted that significant differences can be observed depending on the position of the specimen in the flow (Fig. S2). Lower values are observed at the upper and lowermost ends of the flow, but near-lying specimens show the highest values.

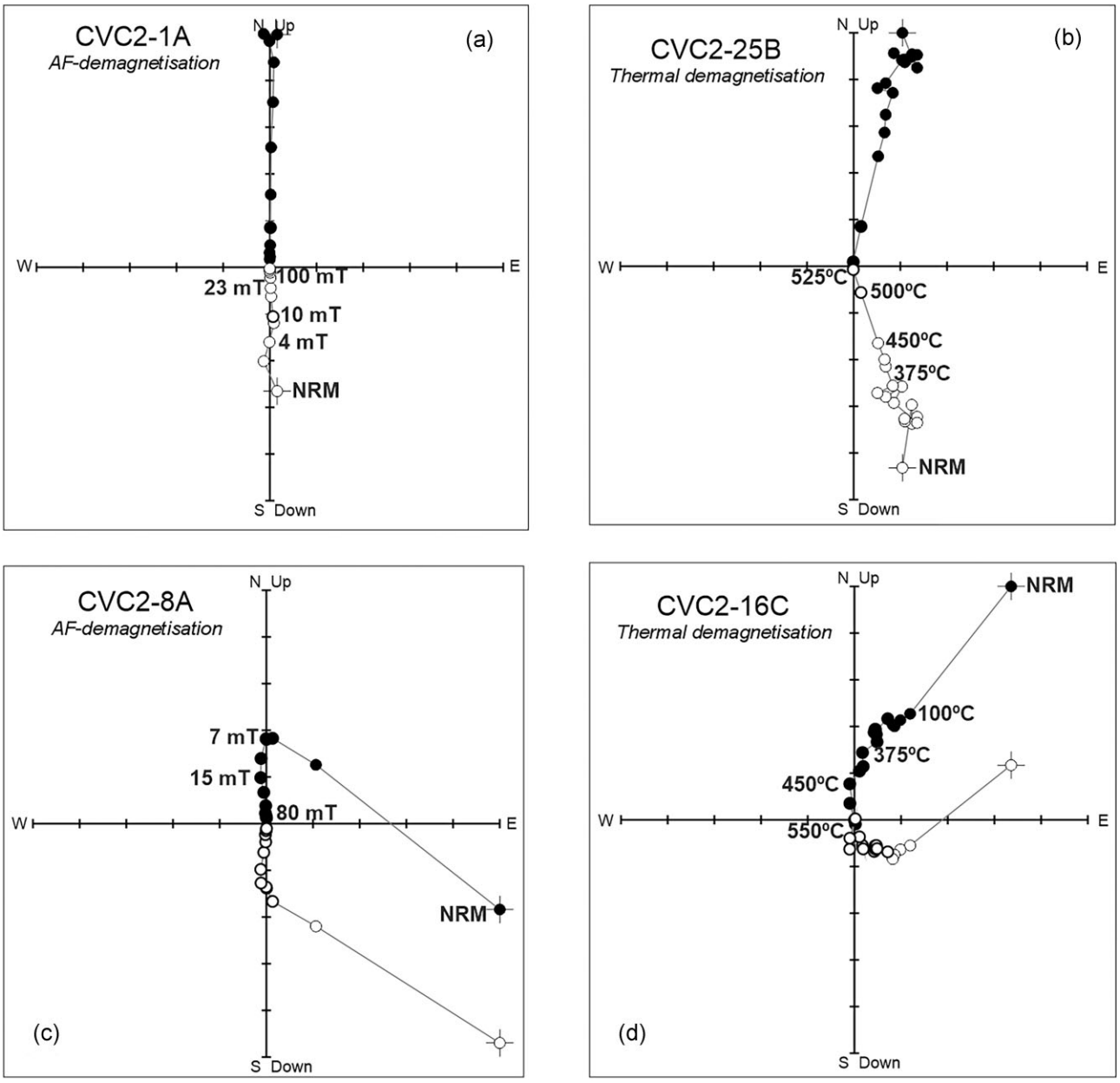

Figure 3. Zijderveld plots. (a) AF- demagnetization of sample CVC2-1A; (b) thermal demagnetization of sample CVC2-25B; (c) AF- demagnetization of sample CVC2-8A; (b) thermal demagnetization of sample CVC2-16C Horizontal projection: closed symbols; vertical projection: open symbols. Plots are shown in the geographic coordinate system.

4. ROCK-MAGNETISM EXPERIMENTS

4.1 Rock-magnetism experiments: methods

Different rock-magnetic measurements were performed to identify the carriers of remanent magnetization and obtain information about their grain size and thermal stability. Experiments including the measurement of thermomagnetic, hysteresis and IRM-acquisition curves, and low-field bulk magnetic susceptibility at two frequencies (470 and 4700 Hz) were carried out at the palaeomagnetic laboratory of the University of Burgos (Spain). First Order Reversal Curves (FORC) were measured in the archaeomagnetism laboratory at National Centre for Research on Human Evolution (CENIEH) in Burgos (Spain).

Magnetic susceptibility was measured at two different frequencies (470 and 4750 Hz) with a MS2B susceptibility meter (Bartington Instruments), and each measurement was repeated three times.

A Variable Field Translation Balance (VFTB) was used at the palaeomagnetic laboratory of the University of Burgos to perform the following measurement sequence: (i) isothermal remanent magnetization (IRM) acquisition curves with a peak field of 1 T; (ii) hysteresis curves; (iii) backfield curves and (iv) thermomagnetic curves. For these experiments one specimen was taken from each core of the flow as well as from two ocean cooled specimens (from the interior and the external crust of the flow). The experiments were performed on crushed specimens, and all were carried out in air.

Thermomagnetic measurements included in all cases strong-field (38 mT) magnetization versus temperature (M_S–T) curves and in most cases also susceptibility versus temperature (k–T) curves. The 38 mT applied field is considered a strong field for the acquisition of induced magnetization during thermomagnetic experiments because it is three orders of magnitude stronger than the EMF. At the beginning of all thermomagnetic experiments, specimens were subjected to a 1 T field, acquiring a (near) saturation remanent magnetization. Subsequently, specimens were heated to a peak temperature of 700 °C and cooled down to room temperature. Subsequently, a second series of hysteresis and backfield measurements was performed on all specimens to record changes occurred after heating. Rock-magnetic measurement data were analysed with the RockMagAnalyzer 1.0 software (Leonhardt 2006).

IRM acquisition experiments for coercivity spectra analysis were carried out with an IM-10–30 impulse magnetizer (ASC Scientific). The samples were subjected to fields ranging from 2 to 1000 mT in 36 IRM-acquisition steps. Two remanence measurements with a 2 G Enterprises cryogenic magnetometer (model 755) were performed for each step: immediately after field application (0 min) and 7 min after field application. Decomposition of the IRM acquisition curve coercivity distribution was performed with the MAX UnMix software (Maxbauer *et al.* 2016). Each coercivity component is characterized by its mean coercivity (peak coercivity of the coercivity distribution) $B_{1/2}$, the dispersion parameter DP, the extrapolated relative contribution of each component to the total magnetization EC and a parameter S describing the curve skewness (Egli 2003).

At the palaeomagnetic laboratory of CENIEH (Burgos, Spain), FORCs were measured to assess the domain states and the presence magnetostatic interactions of ferromagnetic minerals on some representative samples from the flow. Measured samples come from the top, middle and bottom part of the sequence. With the aid of a vibrating sample magnetometer (MicroMag Model 3900, Princeton, noise level $\sim 0.5 \times 10^{-6}$ emu), six first order reversal curve diagrams (FORCs; Pike *et al.* 1999) were obtained. The number of curves measured per sample ranged from 250 to 450, with field increments between 1 and 2.5 mT. The diagrams were plotted using the FORCinel software (Harrison & Feinberg 2008) by applying the optimal smoothing factor calculated by the programme, generally between 5 and 8.

4.2 Results of thermomagnetic experiments

Determination of Curie temperatures from thermomagnetic curves (Petrovský & Kapička 2006) was performed in M_S–T curves with the two-tangent method (Grommé *et al.* 1969) and in k–T curves using inflexion points after susceptibility drops (Table S1). Observed thermomagnetic curves can be divided into four different types of behaviour (H, MH, MxI and L). We will consider magnetization-versus-temperature curves to be reversible if the same remanence-carrying minerals are observed both in the heating and cooling curves and initial and final intensities do not differ more than 20 per cent. M_S–T curves of type H samples (7 of 29; Fig. 4a) generally show a single near-magnetite phase and a relatively high degree of reversibility. However, k–T curves of type H specimens (not measured in all cases) display in addition to magnetite a weak low Curie-temperature phase (<200 °C) which disappears after heating (Fig. 5). This low-T_C phase is not observed in M_S–T curves or can only be intuited after comparison with k–T curves. It seems that a relatively low amount of a low-T_C phase is present in type-H samples but does not contribute significantly to remanence. Type MH curves (2 of 29) show two phases, magnetite, and another one with Curie temperature around 300 °C (Fig. 4b), both in the heating and cooling branch, displaying a high degree of reversibility. Type MxI curves (Fig. 4c), on the other hand, show a clearly irreversible behaviour and were observed in most specimens (18 of 29). They are characterized by the presence of two or three phases in the heating curve: magnetite together with titanomagnetites or titanomaghemites of low (70–200 °C) and intermediate (420–530 °C) Curie temperature. In the cooling curve, only a near-magnetite phase can be observed. Irreversible type L curves (2 of 29, Fig. 4d) were observed only in the samples cooled down in the ocean. They are characterized by a low Curie temperature in the heating curve ($T_C < 200$ °C). Heating produces a near-magnetite phase ($T_C \approx 500$ °C) which is observed in the cooling curve together with the low Curie temperature phase. The Curie temperature of the near-magnetite phases was often somewhat lower in the cooling than in the heating branch of thermomagnetic curves (Table S1), an observation which may be attributed to cation reordering during heating (Bowles *et al.* 2013).

4.3 Results of IRM acquisition experiments

IRM acquisition curves measured with a VFTB show a clear predominance of low coercivity carriers of remanence (Fig. S3, Table S2) and 95 per cent of saturation remanence (SIRM) is reached in fields lower than 150 mT in 75 per cent of the cases (Table S2). Only two samples needed higher applied fields between 200 and 300 mT to reach saturation.

Results of coercivity spectra analysis of IRM acquisition curves are shown on Fig. S4 and Table S3. Coercivity spectra have been fitted for both samples and for different waiting times (0 and 7 min) considering two components of different coercivity. Component 1 displays similar mean coercive field values for both samples and waiting times, with $B_{1/2}$ between 9.3 mT (DP = 0.33) and 14.7 mT (DP = 0.34 mT). The main difference between samples CVC02-04 and CVC02-17 is the relative contribution of component 1 to the total magnetization, between 28 and 33 per cent in CVC02-04 and 70 per cent for CVC02-17. This component can be associated to magnetite grains below the stable SD size, but of sufficient size to be able to acquire a remanence during the duration of the experiments, that is grains at the SP/SD boundary (Spassov *et al.* 2003), or even MD grains.

Component 2, on the other hand, displays different $B_{1/2}$ values and a different relative contribution to remanence in both samples. In the case of sample CVC02-04, $B_{1/2}$ values are similar (37 mT) regardless of the waiting time, with a relative contribution of approximately 70 per cent. Component 2 of sample CVC02-17, however, has a clearly higher mean coercivity (around 55–60 mT) and its contribution to total remanence is lower (30 per cent). This component might be associated with titanomagnetite with differing titanium content and/or degree of oxidation (Dunlop & Özdemir 1997). The high dispersion values could indicate that each component comprises a broad grain size spectrum or even mineralogical substitutions.

4.4 Results of hysteresis measurements

After correction for the dia- and paramagnetic contribution, hysteresis parameters were determined from hysteresis and backfield

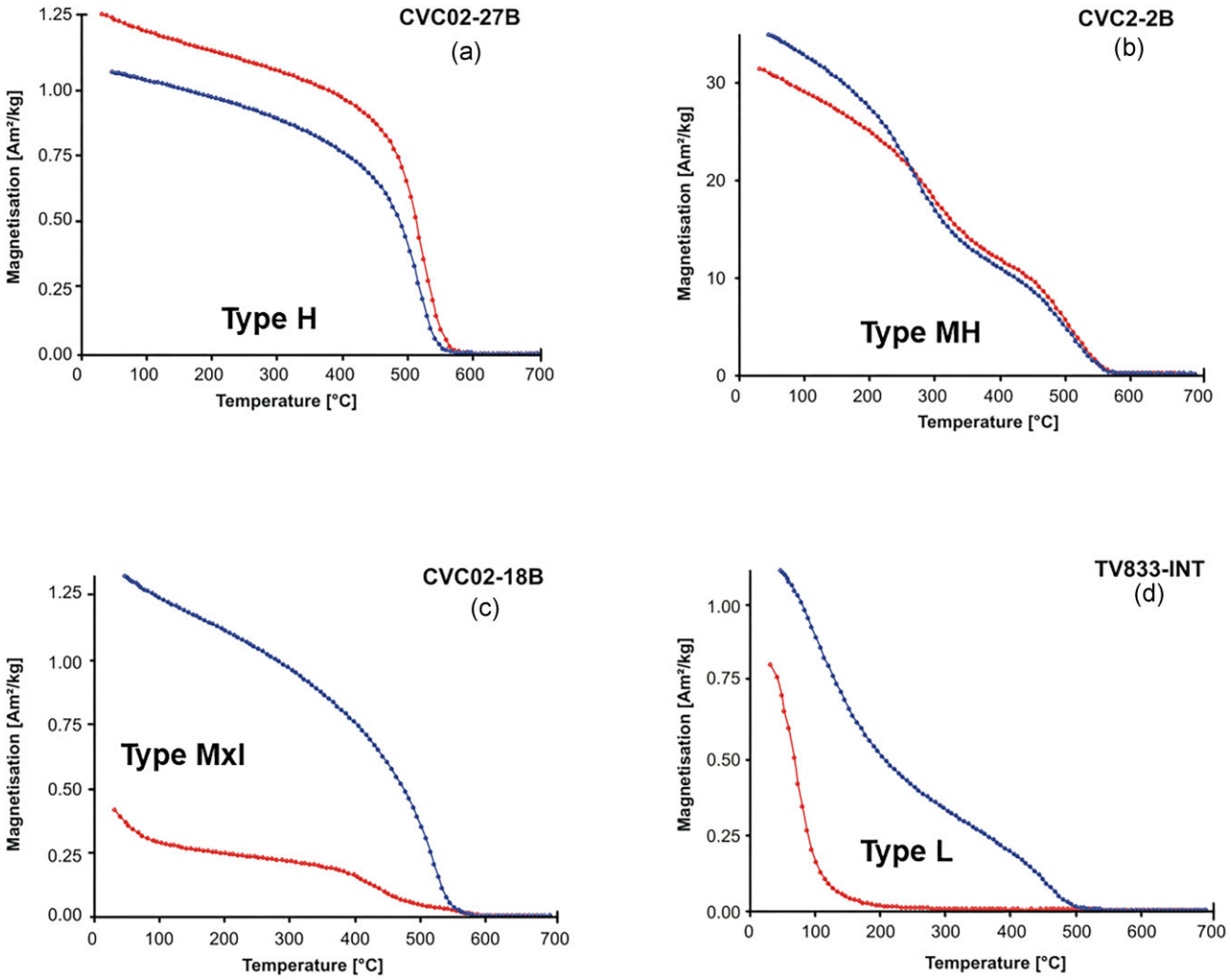

Figure 4. Thermomagnetic curves. Magnetization-vs-temperature curves of representative samples of the four curve types (H, MH, MxI, L) observed (explanation in the text). (a) Type H, sample CVC2-27B; (b) type MH, sample CVC2-2B; (c) type MxI, sample CVC2-18B; (d) type L, sample TV833-INT. Heating curves in red, cooling curves in blue.

curves. In most cases (24 of 29), hysteresis loops are characterized by spreading middles and slouching shoulders (so-called potbellies, Fig. 6a), as indicated by mostly negative values of the shape parameter σ (Fabian 2003; Table S1). Deformed hysteresis curves may originate from mixtures of different magnetic phases and/or domain states (e.g. Pick & Tauxe 1994; Tauxe *et al.* 1996) and thermomagnetic curves have revealed some complexity in the magnetic mineralogy of the studied samples. IRM-acquisition curves showed a clear predominance of low coercivity minerals, and no relation between shape parameter σ and S-300 parameter (Bloemendal *et al.* 1992) or the field at which 95 per cent of SIRM is reached can be recognized (Figs S5a and b). The five remaining samples with positive shape parameters display small values with $\sigma < 0.2$, pointing to a simpler hysteresis behaviour.

Fig. 6(b) shows a Day-diagram (Day *et al*. 1977; Dunlop 2002) with hysteresis parameter ratios of samples from the whole flow transect together with two specimens cooled down in the sea. Information provided by Day diagrams can be often ambiguous, as hysteresis parameter ratios may be influenced by various conditions (Roberts *et al.* 2018). Nevertheless, although all these samples except the two ocean-cooled specimens belong to the same flow, an extreme variability can be observed across the whole plot. There does not seem to exist any clear relationship with their position in the flow besides perhaps sample 2, from the uppermost end of the flow, which displays a somewhat more SD-trending behaviour. It is interesting to note that hysteresis parameter ratios tend to deviate rightwards in the Day-plot from the magnetite SD-MD mixing line (Dunlop 2002) towards the SD-SP mixing line with increase of the (apparent) MD fraction.

Additional evidence about domain state characteristics can be obtained from the relation between shape parameter σ_{HYS} and coercivity ratio B_{RH}/B_{CR} (Fabian 2003). B_{RH} is the positive field value where the difference between both hysteresis branches has decreased from $2M_{RS}$ (saturation remanence) to M_{RS} at $B = 0$. In the SD-MD area, σ_{HYS} is rather independent of grain size and variations suggest the presence of different mineral phases or superparamagnetic (SP) grains (Fabian 2003). On the other hand, while B_{RH}/B_{CR} ratios lower than 1 would point to SP grains, high B_{RH}/B_{CR} ratios suggest the presence of large grains (Fabian 2003). In the present study, σ_{HYS} are mostly negative and show a large variation (Fig. 6c; Table S1), although in the few samples with positive shape parameters this parameter barely changes. The B_{RH}/B_{CR} ratio displays values between 1 and 2 for most samples with negative σ_{HYS} and rather large values for samples with positive σ_{HYS} (Fig. 6c). Thus, shape parameter

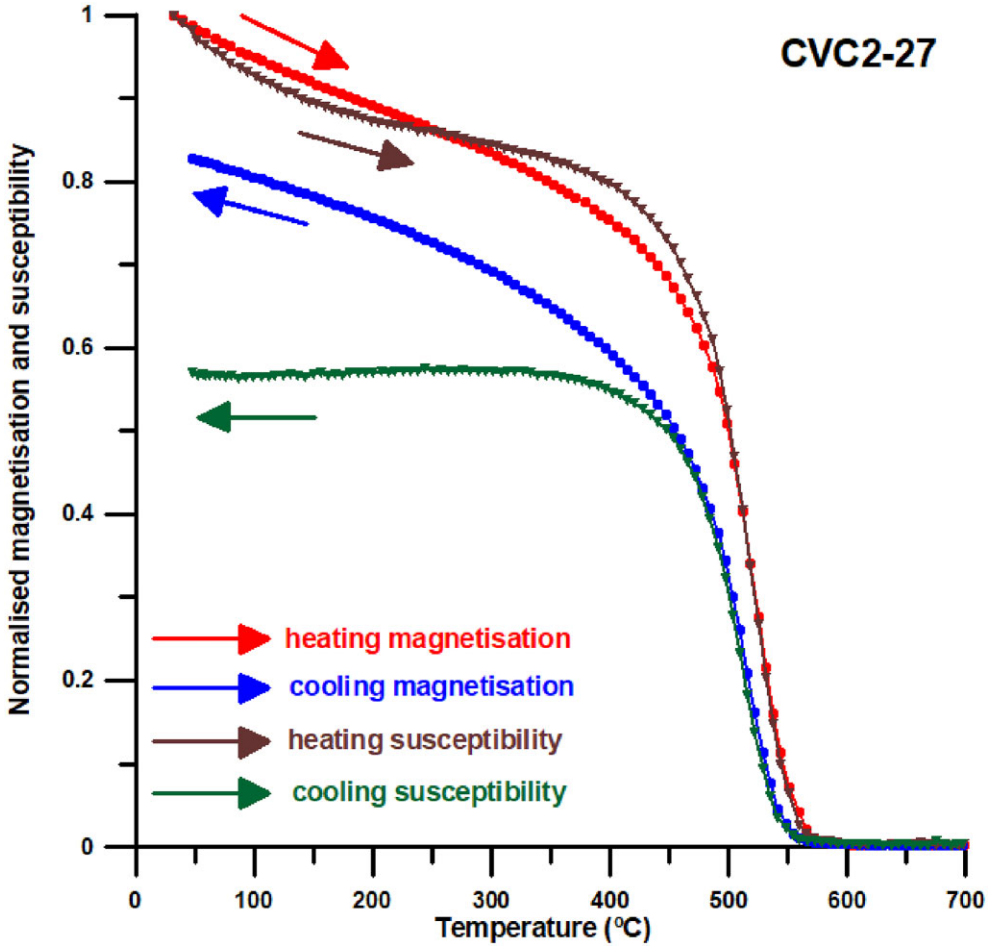

Figure 5. Comparison of thermomagnetic curves. Magnetization-versus-temperature curves (heating in red, cooling in blue) and susceptibility-versus-temperature curves (heating in brown, cooling in green) of type H sample CVC2-27.

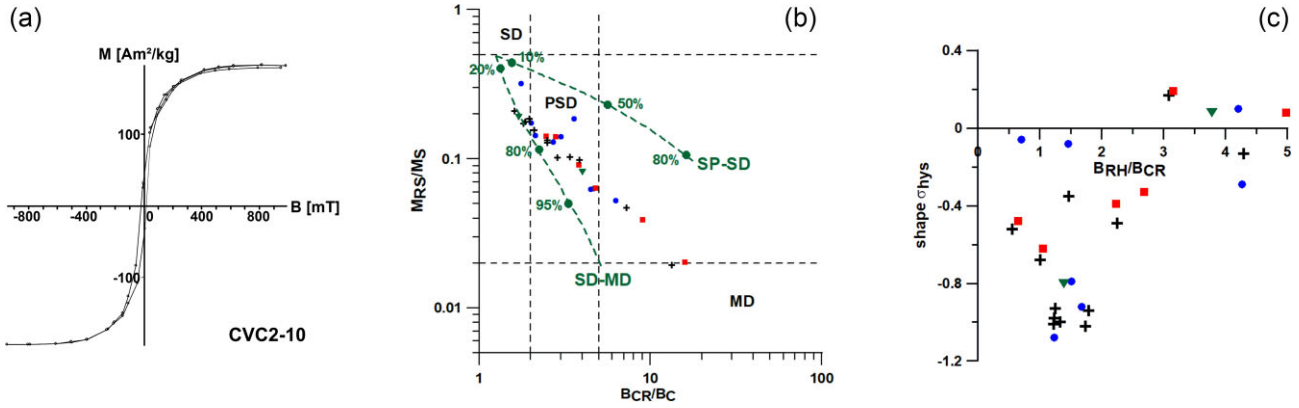

Figure 6. Hysteresis curves results. (a) Hysteresis curve of sample CVC2-10; (b) bi-logarithmic Day-plot (Day et al. 1977; Dunlop 2002) with samples from the December 4 flow (blue, black crosses, red) and ocean-cooled ones (green); SD-MD and SD-SP mixing lines (Dunlop 2002) have been included in the plot; (c) Relation of shape parameter σ (Fabian 2003) and BRH/BCR ratios. Symbols: (i) blue circles: samples CVC2-1 to CVC9, upper part of the flow; black crosses: samples CVC2-10 to CVC21, central part of the flow; Red squares: samples CVC2-22 to CVC27, lower part of the flow; green inverted triangles: ocean cooled samples.

variations seem to be related with the presence of different low-coercivity phases and the larger differences observed in the B_{RH}/B_{CR} ratio might be mainly related with differing mixtures of SD and MD grains. Although data points in the shape parameter—coercivity ratio plot do not show a clear correlation with their position in the flow, specimens from the uppermost part of the flow are generally characterized by lower B_{RH}/B_{CR} ratio values, and thus by a smaller grain size.

After having heated samples to obtain thermomagnetic curves, hysteresis and backfield curves were measured again, revealing

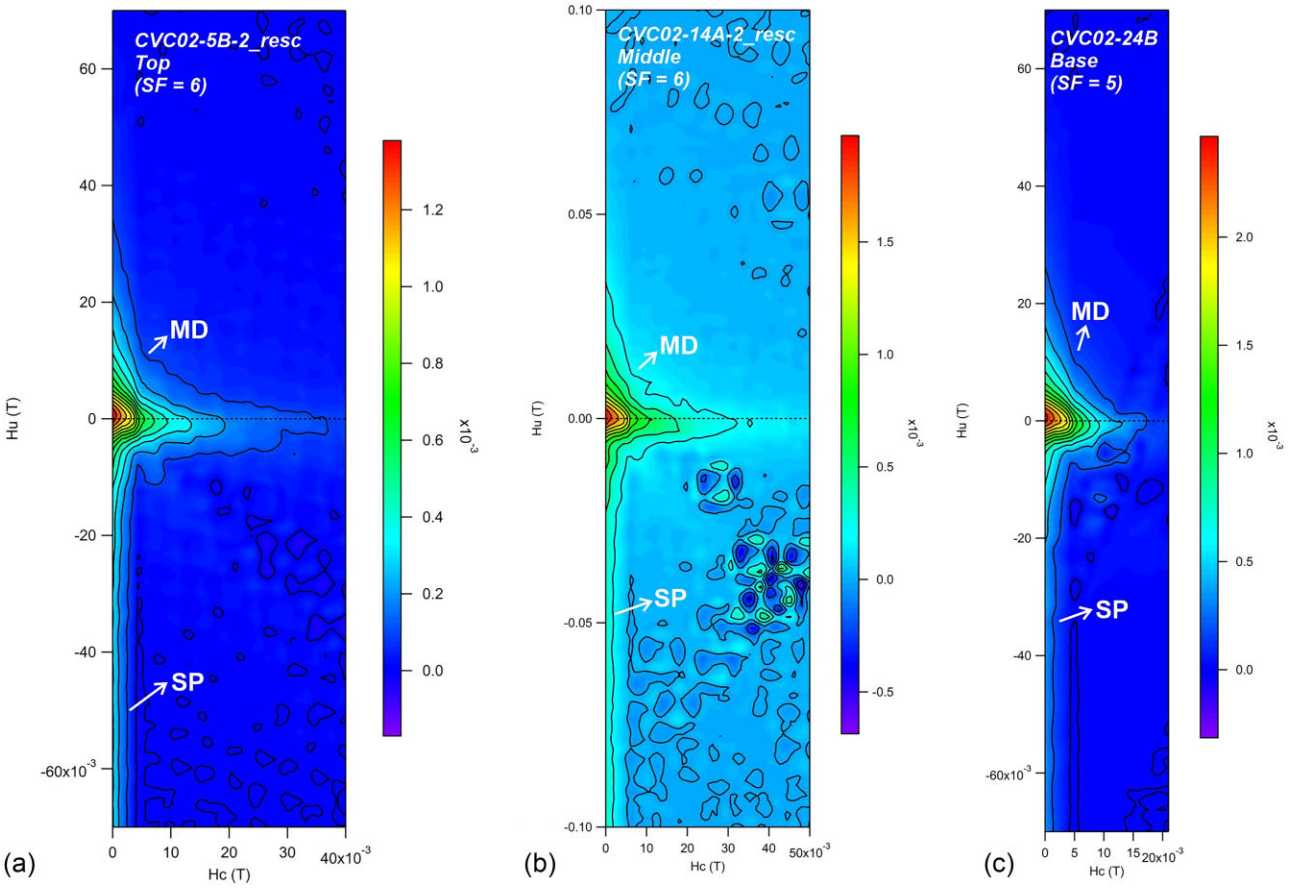

Figure 7. FORC diagrams. Three representative FORC diagrams from the (a) upper, (b) middle and (c) lower part of the sequence. MD = multidomain. SP = superparamagnetic. Sample code and SF (smoothing factor) applied are also indicated. See text for explanation.

a significant variation of hysteresis parameter ratios (Fig. S6; Table S4). Heating to 700 °C tends to reduce the coercivity of remanence to coercivity ratio (B_{CR}/B_C) and increase (sometimes very strongly) the saturation to saturation–remanence ratio (M_S/M_{RS}), making samples, which all contain newly created magnetite due to heating, more SD-like (Fig. S6a). Especially large increases in the magnetization ratio are observed in two samples from the central part of the flow (CVC2-12 and CVC2-13, black crosses in Fig. S6b) and one from the lower part (CVC2-23, red square in Fig. S6b). A strong increase in the coercivity ratio is detected in a specimen from the upper end of the flow (CVC2-2, blue circle in Fig. S6b).

4.5 Results of susceptibility measurements

The relative dependence of the susceptibility on frequency χ_{fd} (per cent) has been calculated with χ_{fd} (per cent) $= 100\cdot(\chi_{lf} - \chi_{hf})/\chi_{lf}$, where χ_{lf} and χ_{hf} are the low and high frequency susceptibilities, respectively. This parameter indicates the contribution of fine magnetite grains near the superparamagnetic/single-domain (SP/SD) boundary (Dearing *et al.* 1996). Results are shown on Table S3.

Frequency dependence of susceptibility χ_{fd} (per cent) for both samples yields a value of 4.8 per cent, pointing towards a non-negligible contribution of magnetite grains near the SP/SD boundary (Dearing *et al.* 1997). These authors consider that in soils such an χ_{fd} (per cent) value would correspond in the case of magnetite to a 30 per cent contribution of grains near the SP/SD boundary. Although this observation cannot be transposed directly to a volcanic lava flow context, the observed χ_{fd} (per cent) results most probably imply a considerable contribution of (titano)magnetite grains in this grain size range.

4.6 First order reversal curves (FORC): results

FORC diagrams confirm the presence of ferromagnetic particles of very low coercivity and no closed contours typical of single-domain grains can be identified. Rather, SP particles (indicated by very low coercivity tails parallel to the *Y*-axis) and MD particles (characterized by open outer contours) seem to coexist (Figs 7a–c). The absence of closed contours in all studied samples suggests that single-domain grains are not present or at least do not dominate magnetization. The degree of magnetostatic interaction, defined by $H_U \neq 0$ and elongated contours with vertical spread (Robert *et al.* 2000), does not seem to be significant. All analysed samples show a strikingly low coercivity ($B_C = 2$–3 mT), and in general, all FORC diagrams exhibit a similar behaviour regardless of their position within the flow.

5. MICROSCOPIC OBSERVATIONS

To closely examine the opaque minerals present in the studied rocks, four thin sections from samples CVC2-02B, CVC2-25A, CVC2-13B and TV833 were selected. They were polished and analysed using a Leica DMRXP optical microscope equipped with both normal and reflected light. Initial observations revealed that the opaque

minerals are uniformly distributed throughout the rock, with most grains being small, under 0.2 mm and generally exhibiting anhedral or subhedral habits. Notably, the largest opaque minerals range from 0.45 to 0.5 mm in maximum dimension, with some rare specimens reaching up to 1 mm in length. The following two samples, CVC2-02B and CVC2-13B, that correspond to the upper central part of the lava flow respectively, have been selected for observation under electron microscope and for conducting EDS (Energy Dispersive Spectroscopy) analysis at University of the Basque Country (UPV/EHU). Thin sections were polished, coated with gold, and then examined with a JEOL JSM-6400 scanning electron microscope (SEM). EDS microanalyses were conducted at a 15 mm working distance using an Oxford Inca Pentafet X3 dispersive X-ray analyser equipped in the SEM. Backscattered electron signals (BSE) operated at 20 kV with a current intensity of 1×10^{-9} A.

In sample 02B, corresponding to the upper part of the lava flow, three types of opaque minerals can be distinguished. First, there are a few examples of significantly larger minerals, up to 500 μm, which are anhedral titanomagnetites with a dendritic texture and low titanium content (Fig. 8a). These display ilmenite exsolutions in the form of Trellis-type lamellae formed by deuteric oxidation at high temperature. Secondly, medium-sized opaques, around 100 μm, are partially included in or in contact with large silicate crystals. These are composed of chromite cores surrounded by an intermediate zone of titanomagnetite and an outer rim rich in titanium (Fig. 8b). In the intermediate titanomagnetite zone, high-temperature exsolution processes form Trellis-type ilmenite lamellae, while the outer titanium-rich rim appears dirtier, with inclusions and small fractures. Opaque minerals with a large variability in size were generally observed. Some are larger than 50 μm, but lastly, the most abundant minerals are less than 10 μm and very often even less than 1 μm in size. They appear dispersed throughout the rock matrix and show evidence of patchy exsolution with ilmenite patches and titanium-poor magnetite zones. All three types of opaque minerals exhibit fine fractures, which can be interpreted as evidence of incipient low-temperature oxidation and the consequent development of maghemite. This process is more evident in the outer rim and the intermediate zone of the crystals with chromite cores, where small shrinkage cracks are more abundant.

In the case of sample 13B, which corresponds to the central zone of the lava flow, all opaque minerals, regardless of their size and morphology, are homogeneous crystals of titanomagnetite, in which compositional variations are barely recognizable (Fig. 8c). In this sample, fine fractures related to an incipient maghemitization process are also recognized, but to a lesser extent than in the previous thin section.

The homogeneous optical appearance of the titanomagnetites does not rule out the possibility that they may be substantially altered (Lied *et al.* 2020).

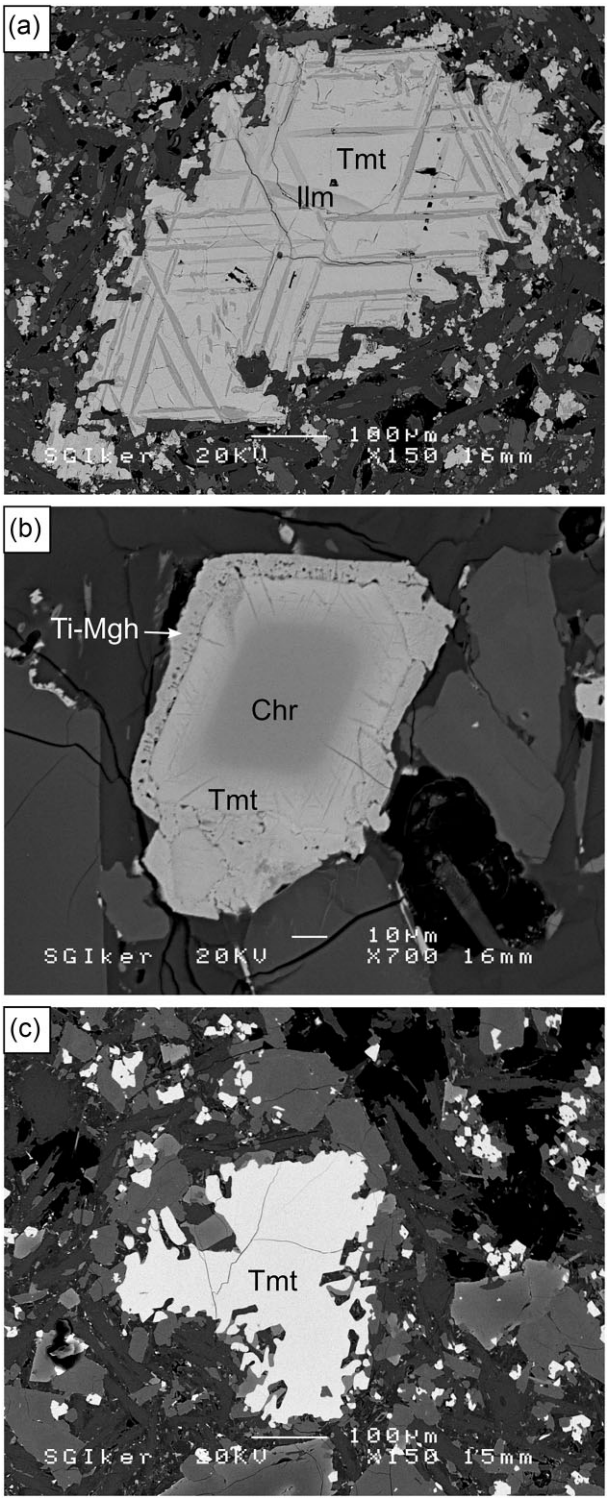

Figure 8. Backscattered electron images. (a) Crystal of titanomagnetite with Trellis-type exsolution lamellae of ilmenite (Ilm) from sample CVC02-02B. (b) Zoned crystal with a chromite core, an intermediate zone of titanomagnetite and an altered rim of titanomaghemite from sample CVC02-02B. (c) Optically homogeneous titanomagnetite crystal from sample CVC02-13B. Tmt: titanomagnetite; Ilm: ilmenite; Chr: chromite; Ti-Mgh: titanomaghemite.

6. PALAEOINTENSITY EXPERIMENTS: METHODS

As outlined in the previous sections, palaeomagnetic and rock-magnetic data obtained from most analysed samples suggest that they are probably unsuitable for palaeointensity determinations, so that in a standard study most probably no palaeointensity experiments would be undertaken in this site. However, to analyse the ability of these rocks to provide a record of the Earth's magnetic field strength and to assess the reliability of the record, we performed palaeointensity determinations with three different

methods: Thellier-Coe (Thellier & Thellier 1959; Coe,1967), multispecimen (Biggin & Poidras 2006; Dekkers & Böhnel 2006) and Tsunakawa-Shaw (Tsunakawa & Shaw 1994; Yamamoto *et al.* 2003).

The Thellier-Coe method was performed on 27 specimens at the University of Burgos (Spain). 25 belonged to the December 4th flow and two were taken from the ocean cooled samples. For the experiment, small rock specimens were fixed into boronsilicate vials and subjected to 14 heating-cooling double steps up to 574 °C, applying a laboratory field of 35 μT, similar to the expected one. Heating and cooling were carried out in an ASC TD-48 single-chamber palaeointensity oven in an argon atmosphere to try to minimize oxidation. We applied 5 pTRM-checks starting at 248 °C and 3 pTRM-tail checks (Riisager *et al.* 2000). Samples were left cooling down naturally, usually overnight during several hours.

Further palaeointensity determinations were carried out at the University of Burgos (Spain) with the multispecimen method (MS), using the routine of Dekkers & Böhnel (2006) (MS-DB) and the fraction correction (MS-FC) and domain-state correction (MS-DSC) protocols proposed by Fabian & Leonhardt (2010). MS determinations were performed on three selected samples from the upper (CVC02-1), intermediate (CVC02-10) and lower (CVC02-26) parts of the flow. All three samples were cut into eight subspecimens and fixed into plaster standard-dimension cylindrical palaeomagnetic specimens. For the experiments, the temperature at which magnetization had lost 70 per cent of its value during thermal demagnetization in palaeomagnetic measurements was chosen. Therefore, MS palaeointensity determinations were carried out at three different temperatures, 460 °C for sample CVC02-1, 400 °C for sample CVC02-16 and 500 °C for sample CVC02-26. A 10 mT AF-demagnetization was performed on the NRM and NRM + pTRM to remove the unstable viscous fraction of the remanence. Laboratory fields were varied in 10 μT steps from 10 to 80 μT. In each heating step, the specimens were heated for 20 min after reaching the temperature selected. Cooling was fan-assisted.

In addition, seven specimens from the upper (CVC02-2, CVC02-6), intermediate (CVC02-16, CVC02-19, CVC02-21) and lower(CVC02-6) parts of the flow, as well as one from the flow cooled under water (TTV-833) were studied in the palaeomagnetic laboratory of the Marine Core Research Institute, Kochi University (Japan), applying the Tsunakawa-Shaw palaeointensity method, according to the procedures detailed in Yamamoto & Tsunakawa (2005). The Tsunakawa-Shaw (TS) method estimates palaeointensities based on coercivity spectra instead of blocking temperature spectra. It uses individual ARM corrections (Rolph & Shaw 1985), a double heating test (Tsunakawa & Shaw 1994) and low temperature demagnetization, which is useful to remove the contribution of MD-like remanences (e.g. Yamamoto *et al.* 2003). The experimental procedure is as follows (Yamamoto *et al.* 2003; Yamamoto & Tsunakawa 2005): (i) NRM is measured. (ii) A specimen is subjected to low temperature demagnetization (LTD) and subsequently stepwise demagnetized by alternating-fields (AF). (iii) The specimen is given an anhysteretic remanent magnetization (ARM) in the direction of the palaeomagnetic component obtained by the previous AF-demagnetization. (iv) The specimen is subjected to LTD and is subsequently stepwise demagnetized by alternating-fields (AF). (v) A first thermoremanent magnetization (TRM1) is given to the specimen. Subsequently, the same procedures as in steps (i)–(iv) are applied. (vi) A second thermoremanent magnetization (TRM2) and the same procedures as in steps (i)–(iv) are applied.

Magnetization was measured with an automated spinner magnetometer with an AF demagnetizer (DSPIN, Natsuhara Giken). LTD was carried out by immerging the specimens in a dewar filled with liquid nitrogen for 10 min and then leaving them heat up outside until room temperature was reached. The whole process was performed in a shielded device. Both TRM1 and TRM2 were acquired in vacuum at a peak temperature of 610 °C in a laboratory field of 40 μT. Specimens were cooled down to room temperature using a fan.

ARMs were imparted after each NRM or TRM demagnetization, approximately parallel to the main NRM or TRM directions, using a DC field of 50 μT with a peak AF of 180 mT. An ARM1 is imparted to calculate TRM1∗ applying the following correction to TRM1:

$$\mathrm{TRM1}^{*} = \mathrm{TRM1} \cdot \frac{\mathrm{ARM0}}{\mathrm{ARM1}}$$

The palaeointensity value is estimated out of a continuous coercitivity interval showing a linear relationship between the NRM–TRM1∗ biplot. To check the validity of this ARM correction and identify possible alterations due to heating, a second TRM (TRM2), is imparted for twice as long as TRM1 to enhance possible thermal alterations, and then demagnetized. An ARM2 is imparted to calculate TRM2∗ applying the following correction to TRM2:

$$\mathrm{TRM2}^{*} = \mathrm{TRM2} \cdot \frac{\mathrm{ARM1}}{\mathrm{ARM2}}$$

A successful check should show a 1:1 relationship over a certain part of the coercivity spectra in the TRM1–TRM2∗ biplot.

7. PALAEOINTENSITY RESULTS

7.1 Palaeointensity results with the Thellier-Coe method

Results obtained with the Thellier-Coe method were analysed with the Thellier-Tool (version 4.22) software (Leonhardt *et al.* 2004). The reliability of a palaeointensity determination depends on a variety of factors. Besides the experimental quality of the data, the extent of alteration during the experiment due to heating and the presence of remanence carried by MD grains must be considered. However, contrary to conventional directional palaeomagnetic studies there is no commonly agreed set of reliability and quality criteria and thresholds. In the present study, successful determinations were selected applying the Thellier tool A and B criteria sets (Leonhardt *et al.* 2004) to distinguish between two quality levels (Q1 and Q2) using the modifications recommended by Paterson *et al.* (2014) except for fraction factor *f*, which was kept at its original value of 0.5 for Q1 determinations. All used criteria and thresholds are shown in Table 2.

Application of this criteria set only yielded five apparently successful determinations out of 27 analysed specimens (Table 2, Fig. 9a). All of them can be ascribed to quality level Q2. Two stem from the lowermost part of the flow and the palaeointensity obtained ($B_{\mathrm{COE}} = 36.9 \pm 3.0$ μT) agrees with the expected field value of 38.7 μT (IGRF-13, Alken *et al.* 2021). Another successful determination was obtained on a specimen sampled very close to the flow upper end (CV2-7), providing a result close to the expected one (within a 10 per cent interval about the expected value if the experimental uncertainty is considered). The two ocean-cooled samples also yield nominally successful determinations which, however, are far from correct (Fig. 9d). The thermomagnetic behaviour of these samples, nonetheless, would have prevented their preselection for palaeointensity determination in a standard study.

Table 2. Palaeointensity results with the Thellier-Coe method.

THELLIER-COE PALEOINTENSITY DETERMINATIONS													
SELECTION CRITERIA		N	f	q	σ/slope	d(CK)	d(TR)	d(t*)	MAD (°)	α (°)			
THRESHOLDS Q1		≥ 5	≥ 0.5	≥ 5	≤ 0.10	≤ 7	≤ 10	≤ 9	≤ 6	≤ 15			
THRESHOLDS Q2		≥ 5	≥ 0.35	≥ 0	≤ 0.15	≤ 9	≤ 20	≤ 99	≤ 15	≤ 15			
SPECIMEN	RANGE	N	f	q	σ/slope	d(CK)	d(TR)	d(t*)	MAD(°)	α (°)	B(μT)	ΔB(μT)	QLTY
CVC02-1	No coherent results												R
CVC02-3	248-511	9	0.623	2.5	0.186	36.2	4.0	51.8	4.8	3.2	98.8	18.4	R
CVC02-4	202-511	10	0.716	0.9	0.456	28.2	2.1	57.0	4.4	5.2	118.8	54.2	R
CVC02-5	No coherent results												
CVC02-6	202-511	10	0.671	9.5	0.059	25.3	1.7	27.4	9.5	15.0	26.8	1.6	R
CVC02-7	202-511	10	0.810	10.5	0.065	7.9	9.7	17.5	4.2	7.0	34.0	2.2	Q2
CVC02-8	150-511	11	0.525	1.7	0.259	28.3	2.1	27.9	8.9	8.1	38.8	9.9	R
CVC02-9	No coherent results												R
CVC02-10	150-511	11	0.553	3.2	0.122	23.2	6.4	34.2	9.2	12.9	19.4	2.4	R
CVC02-11	248-511	9	0.595	2.5	0.190	27.8	1.5	16.2	4.9	5.7	47.7	9.1	R
CVC02-12	299-574	10	0.845	14.1	0.050	14.6	3.8	5.1	9.3	8.6	17.2	0.9	R
CVC02-13	150-511	11	0.804	3.0	0.217	50.2	1.7	16.0	3.7	4.9	172.5	37.5	R
CVC02-14	150-511	11	0.608	4.6	0.116	13.2	1.5	9.7	6.6	7.6	46.0	5.3	R
CVC02-15	248-511	9	0.570	2.3	0.205	23.1	6.6	31.9	8.1	10.8	27.8	5.7	R
CVC02-16	150-511	11	0.590	8.0	0.062	20.9	2.0	2.9	3.2	5.2	30.6	1.9	R
CVC02-17	350-511	7	0.402	1.9	0.167	21.7	6.0	18.7	5.5	2.7	30.6	5.1	R
CVC02-18	202-511	10	0.637	6.6	0.084	25.4	2.9	1.4	7.9	13.0	36.7	3.1	R
CVC02-19	202-511	9	0.378	1.4	0.183	15.9	1.4	2.9	5.6	2.2	34.6	6.3	R
CVC02-20	202-511	10	0.659	3.4	0.162	27.5	5.2	5.2	4.6	4.4	31.3	5.1	R
CVC02-21	202-542	11	0.922	4.1	0.196	29.8	4.6	29.7	5.4	6.6	41.1	8.1	R
CVC02-22	402-542	7	0.892	5.0	0.146	33.2	7.4	10.0	6.5	4.4	35.1	5.1	R
CVC02-23	150-511	11	0.678	2.8	0.197	27.7	6.1	4.9	7.2	8.1	17.4	3.4	R
CVC02-24	150-488	10	0.664	1.7	0.263	41.5	9.9	26.6	11.7	8.0	32.9	8.6	R
CVC02-26	350-574	9	0.893	7.9	0.040	7.9	1.9	2.1	4.5	0.7	36.9	1.5	Q2
CVC02-27	350-511	7	0.381	3.1	0.092	5.7	0.6	1.3	3.8	9.9	39.9	3.7	Q2
TV832 (int)	150-402	6	0.413	2.2	0.115	4.0	1.2	0.0	4.1	1.8	94.4	10.9	Q2
TV833 (ext)	150-350	5	0.639	5.6	0.026	4.5	3.3	47.1	3.8	0.9	79.5	2.0	Q2

Selection criteria and threshold values for class Q1 and Q2. *N*: number of NRM-pTRM points used for palaeointensity determination; *f*: fraction of extrapolated NRM used; *f* is referred to the so-called 'true NRM', which is the intersection between linear fit and *y*-axis (Leonhardt *et al.* 2004); *q*: quality factor (Coe *et al.* 1978); σ/slope: ratio of the standard error of the slope and the slope of the NRM-TRM diagram; d(CK): difference between the pTRM check and original TRM value at a given temperature normalized to the TRM (Leonhardt *et al.* 2000); *d*(TR): relative intensity difference after a repeated demagnetization to check to what extent a pTRM(T_0, T_i) is removed during a zero-field heating-cooling cycle between T_0 and T_i; *d*(*t*∗): tail parameter (Leonhardt *et al.* 2004) to check, which measures the extent of a pTRM-tail after correction for angular dependence; MAD: Mean angular deviation of NRM end-point directions at each step obtained from palaeointensity experiments; α: angle between the vector average of the data selected for palaeointensity determination and the principal component of the data. Thellier-Coe results: SPECIMEN: specimen name; RANGE: temperature interval in °C used for palaeointensity determination; *B* and Δ*B*: palaeointensity estimate and standard error for a single specimen; standard error of the palaeointensity estimate is calculated by the product of the standard error of the best-fitting line in the Arai plot and the laboratory field. QLTY: quality level of palaeointensity determination (R = rejected). Thresholds being met at Q1 level by specimens for different criteria are shown in light yellow. Thresholds being met at Q2 level by specimens for different criteria are shown in orange. Thresholds not being met by specimens for different criteria are shown in light red. Palaeointensity results agreeing with expected intensity are shown in dark green. Palaeointensity results agreeing with expected intensity allowing a 15 per cent interval about the expected IGRF intensity are shown in light green.

Table 2 shows palaeointensity results and selection criteria values for almost all analysed samples, except for three cases, where no coherent results were observed. In many other cases, although Arai plots are of rather poor quality (Figs 9b and c), we attempted to retrieve a palaeointensity value by analysing linear sections in Arai plots and the corresponding Zijderveld diagrams. As shown by table 2, most unsuccessful determinations can be ascribed to alteration because of negative pTRM-checks [selection criterion d(CK)], in accordance with many type-MxI irreversible thermomagnetic curves observed. On the other hand, the high data scatter around the best-fitting line (σ/slope in Table 2) reflecting rather disordered Arai diagrams is also responsible for most rejections. This behaviour might be influenced by the fact that many specimens were characterized by the presence of a significant fraction of MD and SP grains which could have produced distorted measurements.

7.2 Palaeointensity results with the multispecimen method

Multispecimen palaeointensity results were analysed with the palaeointensity.org (Monster *et al.* 2015b; Béguin *et al.* 2020) online open-source application. In the case of multispecimen determinations, this software allows to perform an alignment correction when declination and inclination of the samples at different steps differ from the original NRM and in this study we applied this correction.

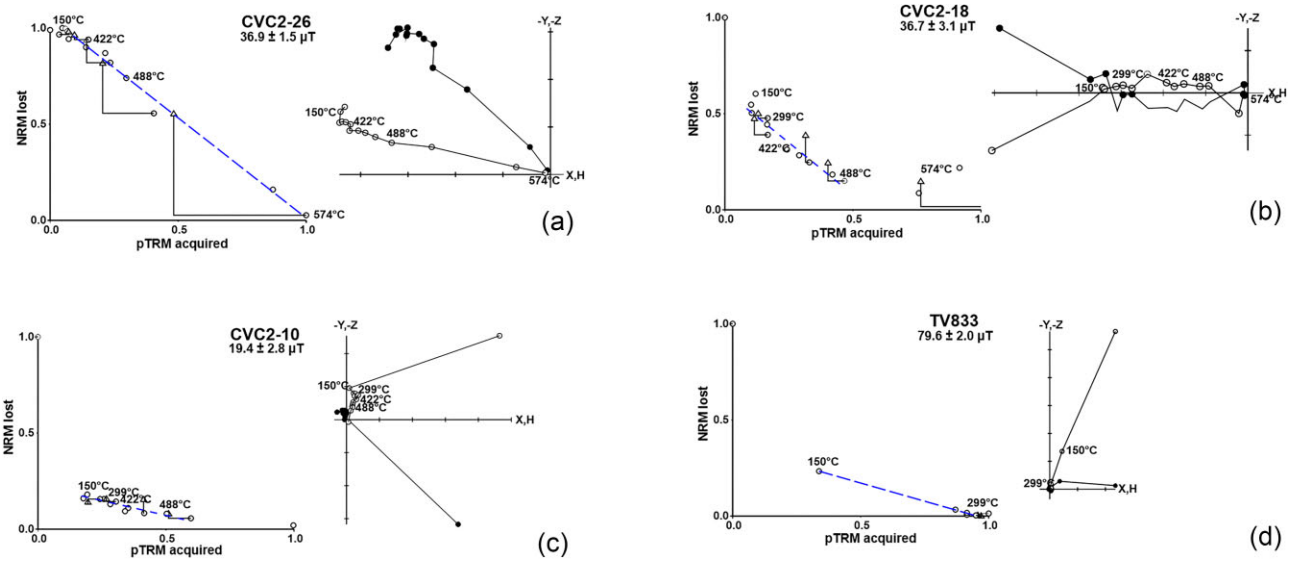

Figure 9. Thellier-Coe palaeointensity determinations. Arai and Zijderveld plots (in sample coordinates) are shown for four selected samples. (a) Successful determination on flow sample CVC2-26. (b) Rejected determination on flow sample CVC2-18. A tentative palaeointensity determination has been performed without taking into account quality criteria thresholds (see text). (c) Rejected determination on flow sample CVC2-10. A tentative palaeointensity determination has been performed without taking into account quality criteria thresholds (see text). (d) Formally successful determination on ocean cooled sample TV833. The palaeointensity obtained strongly differs from the actual value.

For the interpretation of palaeointensity data, parameter α (a constant to calculate the contribution of the domain state effect) was set to 0.5 for all three determinations, as recommended by Fabian & Leonhardt (2010).

Selection criteria for reliable determinations and thresholds are shown on Table 3. They allow to distinguish between two quality levels Q1 and Q2. For the relative alteration error value $\varepsilon_{\rm alt}$ (Fabian & Leonhardt *et al.* 2010) a threshold $\varepsilon_{\rm alt} = 3$ per cent as suggested by De Groot *et al.* (2013) and Monster *et al.* (2015b) is required for Q1 determinations and a less stringent $\varepsilon_{\rm alt} = 10$ per cent (Sánchez-Moreno *et al.* 2021) for Q2 determinations. To check whether the linear fit intersects the ordinate axis through (0,−1), Q1 determinations require a coincidence within 10 per cent (Monster *et al.* 2015b) and/or within error and Q2 determinations within 15 per cent and/or within error (Calvo-Rathert *et al.* 2021).

Table 3 and Fig. 10 show the results of multispecimen determinations. In samples CV2-1B (uppermost part of the flow) and CV2-10A (intermediate part of the flow) data from two specimens clearly deviating from the general trend were not included in the palaeointensity calculation. In sample CVC2-26C, data from two specimens were omitted because of their very high alteration error $\varepsilon_{\rm alt}$. Domain-state corrected determinations yielded the more reliable results, and for all three samples successful determinations of quality Q2 were obtained. However, none of the samples yielded results close to the $B = 38.7\mu$T field at the site location during the eruption (IGRF-13, Alken *et al.* 2021).

7.3 Tsunakawa-Shaw palaeointensity determinations

To estimate absolute palaeointensity values, results were analysed using the python code by Yamamoto *et al.* (2022) with the PmagPy software package (Tauxe *et al.* 2016) and the following selection criteria and thresholds were applied for the TRM1-TRM2∗ biplots (Table 4): fraction $f_{\rm T} \geq 0.15$, correlation coefficient $r_{\rm T} \geq 0.995$ and $0.95 \leq$ slope $T \leq 1.05$. The criteria for the NRM-TRM1∗ biplot were the following: fraction $f_{\rm N} \geq 0.15$, and correlation coefficient $r_{\rm N} \geq 0.995$ (e.g. Kitahara *et al.* 2018).

Results are shown on Table 4. Successful determinations were achieved on four specimens from the lava flow, while two lava flow specimens and the one cooled under water were discarded. For the successful specimens, ARM correction seems to work well to obtain a linear continuous coercivity interval from where to estimate an absolute palaeointensity value (Fig. 11). In addition, the LTD treatment might have demagnetized a strong viscous component observed in many samples. The specimens that did not pass the selection criteria had a curvature parameter (k') larger than 0.2 in some of their demagnetization ratios (Lloyd 2021), as shown in Table 4. For this reason, their palaeointensity results were discarded. It is remarkable that, in the case of specimens CVC02-21 and TTV833, the MDF value of the NRM demagnetization is 5 mT, so that these strongly viscous samples do not seem suitable for palaeointensity experiments.

8. DISCUSSION OF RESULTS

8.1. Palaeomagnetic results

As shown by rockmagnetic (e.g. Figs 4 and 6b), palaeomagnetic (Fig. 3) and viscosity (Fig. S2) experiments, the samples taken along the 2.2 m thick December 4 flow are characterized by a remarkable variability regarding thermomagnetic and hysteresis properties of the carriers of remanence as well as the characteristics of the palaeomagnetic signal. The most notable aspect of the latter is the presence of an often-strong viscous component. The weakest viscous overprints are observed in the lowermost end of the flow, but also samples from the upper end as well as some of the central part show a viscous component of more moderate intensity. On a Day diagram (fig. 6b) samples plot throughout the entire diagram, being in the SD, PSD and MD areas without any specific relation with their position in the flow. In fact, they tend to

Table 3. Palaeointensity results with the multispecimen (MS) method.

				Multispecimen palaeointensity determinations						
				n	ε_{alt} (per cent)		r^2		$\lvert\Delta b\rvert$ and/or within error	
	Thresholds Q1			≥ 5	≤ 3		≥ 0.900		0.1	
	Thresholds Q2			≥ 4	≤ 10		≥ 0.850		0.15	
Specimen	Protocol	T (°C)	B (μT)	B_{min} (μT)	B_{max} (μT)	n (N)	ε_{alt} (per cent)	r^2	Δb	QLTY
CVC02-1	DB	460	4.9	-	14.2	7(8)	-	0.762	-	
	DSC	460	15.4	0.6	26.6	7(8)	-5.9	0.875	-1.37/YES	Q2
CVC02-10	DB	400	21.0	17.1	23.2	6(8)	-	0.981	-	
	DSC	400	17.4	13.6	20.7	6(8)	-5.6	0.948	0.13/YES	Q2
CVC02-26	DB	500	26.6	25.5	30.1	6(8)	-	0.996	-	
	DSC	500	21.2	16.8	25.9	6(8)	-7.4	0.977	-0.26/YES	Q2

Selection criteria and threshold values for class Q1 and Q2. n: number of specimens used for palaeointensity determination; ε_{alt}: Average alteration parameter; r^2: quality of the linear least-squares fit; $\lvert\Delta b\rvert$: check of whether the linear fit intersects the ordinate axis through (0.−1) within 10 per cent (Q1) or 15 per cent (Q2) and/or within error (Yes or No). Multispecimen results. B: palaeointensity results. PROTOCOL: original uncorrected MS (DB) and domain state corrected (DSC) protocol; B_{Min} and B_{Max}: palaeointensity determination uncertainty bounds. QLTY: quality level of palaeointensity determination.

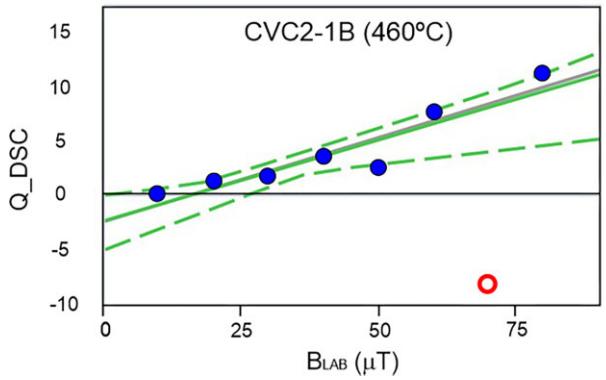

Figure 10. Multispecimen palaeointensity determinations. Domain-state corrected multispecimen palaeointensity determination on sample CVC2-1B (performed at 460 °C). Closed blue dots represent used and open red dots rejected data.

deviate in the Day-plot from the magnetite SD-MD mixing line towards the SD-SP mixing line. Day diagrams have been criticized because of the ambiguity of the information that they can provide, because hysteresis parameter ratios may be influenced by various conditions (Roberts *et al.* 2018). Nevertheless, in this case a Day-plot seems to be an adequate means to at least reflect the variability of the observed (palaeo)magnetic characteristics of the samples.

As shown by Fig. S1, calculated mean directions agree very well with the expected IGRF value, regardless of if they have been calculated with only thermally, only AF-demagnetized or all studied samples. A closer look at the data (Table 1), however, shows that in several cases significant differences are obtained on specimens of the same core with AF or thermal demagnetization, with angular differences sometimes larger than 10 or 20°. Both demagnetization techniques seem to show different effectiveness in separating TRM and viscous components for different samples. An average over a sufficiently large amount of data obtained with both techniques bypasses this problem, but a mean direction obtained over a low sample number and/or a biased sample distribution, for instance, due to sampling of a limited easier accessible part of the flow, could provide incorrect results.

8.2 Unstable magnetization behaviour

Palaeomagnetic experiments performed on the December 4 lava flow samples have shown that the palaeomagnetic signal includes a characteristic component which agrees well with the expected field direction and a secondary, often rather strong component, which can be removed at very low AF demagnetization steps between 2 and 9 mT and, except for a few cases, at low temperatures between 175 and 275 °C. The direction of this secondary component varies among different cores and also differs between specimens from the same core subjected to different demagnetization treatment. Considering these observations and the very young age of the lava flow, it seems that this secondary component has been acquired during a short time, possibly during storage but perhaps also during experimental procedures.

In order to analyse the origin of this component, several specific experiments have been performed to obtain information about the grain size of remanence carriers. Analysis of hysteresis parameter-ratios with a Day plot (Fig. 6b) is not very informative due to the multiplicity of factors which can affect the observations, but it is interesting to note that results plot near the magnetite SD-MD mixing line (Dunlop 2002), but deviating towards the SD-SP mixing line. Frequency dependent susceptibility measurements point towards a significant contribution of grains near the SP/SD boundary. Analysis of coercivity spectra of IRM-acquisition curves suggests the presence of two components of different coercivity. One of these components is characterized by very low coercivities (<15 mT) and can be associated to magnetite grains below the stable SD size, but of sufficient size to be able to acquire a remanence during the duration of the experiments (grains at the SP/SD boundary or MD grains). The other component is also characterized by low coercivities (40–60 mT) and might be associated with titanomagnetite with differing titanium content and/or degree of oxidation. High dispersion values would point towards a broad grain size spectrum. FORC diagrams confirm the presence of particles of very low coercivity (B_C = 2–3 mT). SP particles (indicated by very low coercivity tails parallel to the *Y*-axis) and MD particles (characterized by open outer contours) seem to coexist.

All these experiments suggest that this lava flow contains a larger than usual fraction of ferromagnetic (s.l.) grains of very low coercivity. These grains would be responsible of the presence of rather unstable magnetization components which are easily erased by low fields in AF-demagnetization. In addition, a significant contribution

Table 4. Palaeointensity results with the Tsunakawa-Shaw method.

				Tsunakawa-Shaw palaeointensity determinations								
	Criteria Thresholds			f_N ≥ 0.15	r_N ≥ 0.995	$Slope_T$ 0.95–1.05	f_T ≥ 0.15	r_T ≥ 0.995	$k'_{NRM/TRM1*}$ ≤ 0.2	$k'_{NRM/ARM0}$ ≤ 0.2	$k'_{TRM1/ARM1}$ ≤ 0.2	$k'_{TRM2/ARM2}$ ≤ 0.2
Specimen	$B_{min} - B_{max}$ (mT)	f_N	r_N	$Slope_T$	f_T	r_T	$k'_{NRM/TRM1*}$	$k'_{NRM/ARM0}$	$k'_{TRM1/ARM1}$	$k'_{TRM2/ARM2}$	B (μT)	ΔB (μT)
CVC02-02	22- 180	0.233	0.999	0.959	0.960	0.999	0.074	0.100	0.018	0.012	34.9	0.3
CVC02-06	20–180	0.184	1.000	1.039	0.677	1.000	0.012	0.171	0.174	0.164	37.7	0.2
CVC02-16	14–110	0.518	0.997	1.040	0.808	1.000	0.119	0.084	0.055	0.089	36.9	0.6
CVC02-19	26–180	0.299	0.999	1.046	0.626	0.999	0.082	0.000	0.199	0.303	23.6*	0.2
CVC02-21	20–95	0.271	0.995	1.042	0.698	0.999	0.273	0.004	0.314	0.261	26.3*	0.5
CVC02-25	24–180	0.337	0.998	1.033	0.363	0.997	0.041	0.000	0.014	0.033	38.1	0.4
TV833	95–170	0.076	0.902	0.934	0.989	0.995	0.000	0.239	0.000	0.114	16.0*	2.9

Selection criteria and threshold values. f_N: fraction used for the best-fitting line on the NRM-TRM1* plot; r_N: correlation coefficient for the best-fitting line on the NRM-TRM1* plot; $Slope_T$: slope of TRM1-TRM2* of the second heating; f_T: fraction used for the best-fitting line on the TRM1-TRM2* of the second heating; r_T: correlation coefficient for the best-fitting line on the TRM1-TRM2* of the second heating (e.g. Kitahara *et al.* 2018). *k*': curvature parameter of the NRM-TRM1*, NRM-ARM0, TRM/ARM1 and TRM2/ARM2 plots. Tsunakawa-Shaw palaeointensity determinations. B_{min}–B_{max}: alternating field demagnetization range (in mT) selected for each palaeointensity determination; B and ΔB: palaeointensity estimate and uncertainty.

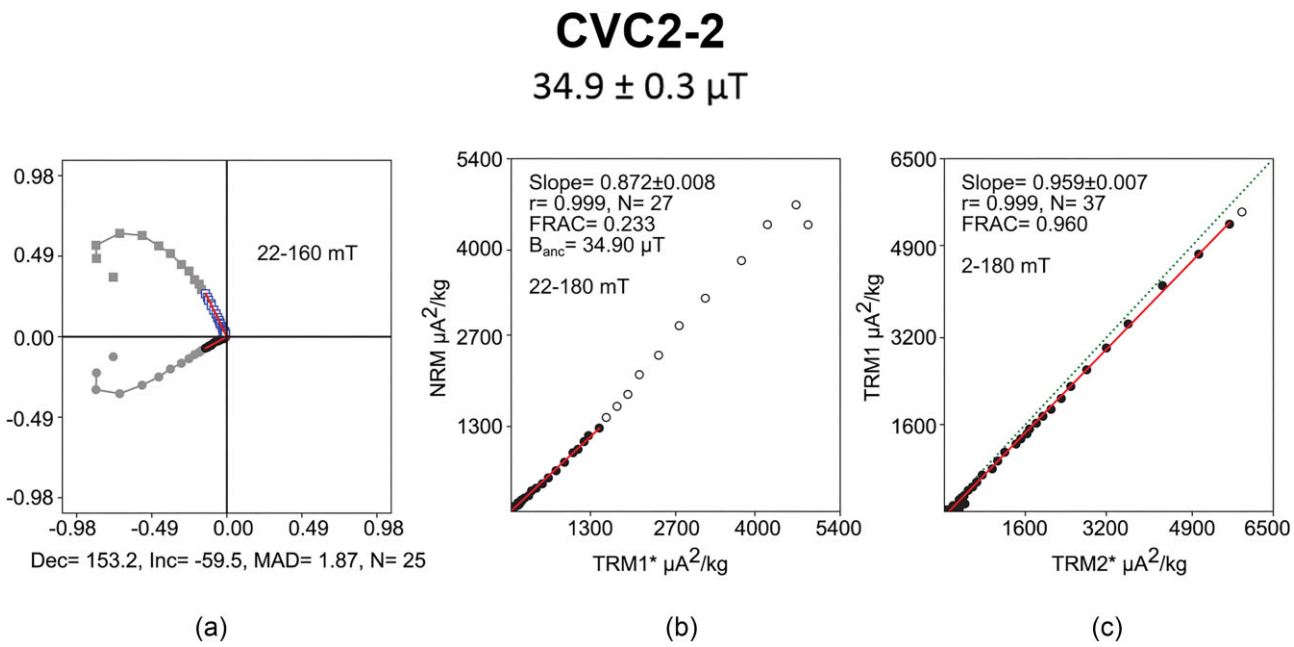

Figure 11. Tsunakawa-Shaw palaeointensity determinations. Successful Tsunakawa-Shaw palaeointensity determination for specimen CVC2-02, using the python code by Yamamoto *et al.* (2022) with the PmagPy software package (Tauxe *et al.* 2016); (a) Orthogonal NRM demagnetization diagram during the initial progressive alternating field demagnetization. The first point (not connected by the line) shows the NRM value before LTD demagnetization prior to progressive AF demagnetization; (b) Final Arai plot for palaeointensity determination and (c) TRM1 versus corrected TRM2, which shows possible temperature alterations as well as the suitability of the applied ARM correction.

of grains near the SP/SD boundary could be responsible for a certain amount of distorted remanence measurements.

8.3 Palaeointensity results with the Thellier-Coe method

Despite the very low success rate obtained with Thellier-Coe palaeointensity determinations, Table 2 shows that almost all analysed samples at least provided data with enough coherence such as to allow performing a tentative analysis without considering any selection or reliability parameters, just looking for linear sections in Arai plots and corresponding Zijderveld plots. If the results obtained with this approach (Table 2) are compared with the expected IGRF intensity at the eruption ($B_{\mathrm{IGRF}} = 38.7\ \mu$T) a considerable agreement can be observed. From 25 determinations performed on the flow, 3 did not provide any coherent results and 9 (36 per cent) agreed with the expected field. If a 15 per cent interval about the expected IGRF intensity is allowed, 6 more determinations show an agreement, yielding a (virtual) success rate of 60 per cent. Negative pTRM-checks might be not only related to alteration. If considered together with scattered and disordered Arai diagrams they could also be related to the fact that many specimens are characterized by the presence of a significant fraction of MD and SP grains, as shown by rock-magnetic experiments. During measurements with the cryogenic magnetometer, samples are stored in a μ-metal shielding. However, as measurements were not carried out in a shielded room, transport from the palaeointensity furnace to the magnetometer exposes samples to the EMF in the laboratory. Subsequent insertion into the sample-holder of the magnetometer also implies a short exposure to a field weakened by Helmholtz coils in a small measurement area. However, despite the apparent acquisition of unstable magnetizations during measurements, the necessary information to retrieve the actual field seems to be still present in many of the analysed samples yielding unsuccessful determinations.

8.3 Palaeointensity results with the multispecimen method

All three samples yield formally successful determinations, with moderately low $\varepsilon_{\mathrm{alt}}$ between 5.6 and 7.4 per cent and linear fits of good (CV2-10AB and CV2-26C) or reasonable (CV2-1B) quality. As for the Δb difference, the CVC2-01B determination shows the farthest y-axis cut-off, but still fulfils the proposed selection criteria. However, none of the MSP-DB or MSP-DSC determinations yields results close to the $B = 38.7\ \mu$T field at the site location during the eruption (IGRF-13, Alken *et al.* 2021). The closest result is obtained in sample CV2-26C, from the lowermost part of the flow, but all three MSP determinations clearly underestimate the expected value. Most probably these determinations are also affected by the presence of a large fraction of MD and SP grains, and a strong viscous component. The small number of analysed specimens, because not enough samples were available, does not allow to draw any firmly based conclusion.

8.4 Tsunakawa-Shaw palaeointensity determinations

All successful palaeointensity determinations from the lava flow outcrop (CVC02-02, CVC02-06, CVC02-16 and CVC02-25) showed a good agreement with the expected field intensity $B = 38.7$mT, yielding a mean value of average of (36.9 $\pm$ 1.4) μT (Table 4). Our correct palaeointensity results obtained with the Tsunakawa-Shaw method might be explained with the fact that samples are initially subjected to liquid nitrogen temperatures in a field-free space, demagnetizing remanence carried by MD-grains and thus 'turning off' the effect of the very strong viscous component

observed in many of the samples. Usefulness of LTD in palaeointensity determination is discussed in Yamamoto *et al.* (2022) in more detail. In addition, the curvature parameter k' has discarded specimens that yielded very low palaeointensity determinations, not compatible with the expected field. This ensures the quality of the obtained results with the selection criteria applied in our study.

On the other hand, the position of the non-successful specimens from the lava flow section was the mid part of the lava flow outcrop. For this reason, these discarded specimens could perhaps contain larger MD magnetite grains due to a slower cooling occurred in this part of the lava flow.

8.5 Multimethod palaeointensity results

The multimethod approach is based on the premise that an agreement of results obtained with different determination methods should be a robust reliability criterium for successful determinations, because it would be highly improbable to find an agreement between results of wrong determinations.

Only five samples fulfilled selection criteria for Thellier-Coe determinations, all at a Q2 quality level. Three belonged to the December 4 flow and two to the ocean cooled samples. The mean palaeointensity result obtained from the three December 4 flow specimens yields a result $B_{\mathrm{COE}} = (36.9 \pm 3.0)\ \mu$T, with a relatively low within-site variation.

On the other hand, all three multispecimen determinations met reliability criteria at a Q2 level, with all three samples belonging to the December 4 flow. Tsunakawa-Shaw determinations yielded successful determinations in four out of seven determinations, specifically, on samples from the December 4 flow, yielding a mean value of $B_{\mathrm{TS}} = (36.9 \pm 1.4)\ \mu$T. One of the rejected determinations was not performed on a sample from the December 4 flow but on an underwater-cooled sample.

To compare results obtained with different methods, we considered that two palaeointensity determinations yielded the same result if the difference between them was less than 15 per cent of the Thellier-Coe result. This condition is fulfilled for the comparison of results obtained with the Tsunakawa-Shaw and Thellier-Coe methods. However, all three multispecimen determinations underestimate this value. In a standard palaeointensity study, the fact that the Thellier-Coe and Tsunakawa-Shaw results reflect the actual field value would be unknown. Nevertheless, their agreement would be a robust indication for the correctness of their common result and would lead us to discard the multispecimen result.

If all seven accepted palaeointensity determinations are given the same weight, a mean final multimethod palaeointensity result $B = (36.9 \pm 2.0)\ \mu$T is obtained, which can be considered a good estimation of the actual field intensity ($B_{\mathrm{IGRF}} = 38.7\ \mu$T).

9. CONCLUSIONS

A palaeomagnetic and palaeointensity study including rockmagnetic experiments has been carried out on 27 cores sampled from top to bottom across a lava flow erupted on December 4th in the island of La Palma (Canary Islands, Spain). Rockmagnetic experiments revealed a considerable variability of magnetic properties across a 2.2 m thick flow, pointing towards a varying degree of mixture of magnetite and/or titanomagnetite of different grain size, probably related to different cooling speed and conditions. In addition, it has been observed that the studied lava flow contains a large fraction of very low coercivity grains (MD and SP/SD boundary), which would be responsible of the presence of rather unstable magnetization components.

Despite the presence of a strong secondary component in many cores, the mean palaeomagnetic direction of all cores agrees very well with the expected IGRF value, also if the analysis is performed separately for thermally or AF-demagnetized specimens. Nevertheless, significant differences are observed on specimens of the same cores between the results obtained with both techniques, and angular differences sometimes amount to 10 or 20°. A mean direction obtained over a low number of samples, specimens demagnetized only using one technique and/or a biased sample distribution due to sampling of a limited easier accessible part of the flow, could provide incorrect results.

Palaeointensity experiments with the Thellier-Coe method in the December 4th lava flow yielded a very low success rate, as only 3 of 25 determinations (12 per cent) provided results fulfilling selection criteria. These results agreed with the expected field value of 38.7 μT (IGRF-13). Performing an informal analysis of linear sections in Arai plots and the corresponding Zijderveld diagrams without considering criteria thresholds yielded palaeointensity results agreeing with the expected field intensity in 60 per cent of the specimens. It could be possible that negative pTRM-checks are not only due to alteration but are also artificially produced during measurements by unstable magnetization due to very low-coercivity grains. Multispecimen determinations performed on three samples provided formally successful determinations which largely underestimated the expected field intensity, although the small amount of available data hinders a more thorough analysis. On the other hand, four Tsunakawa-Shaw determinations performed on samples from the flow yielded correct results. Low-temperature demagnetization of MD grains was included in the Tsunakawa-Shaw protocol and seems to have been helpful for obtaining reliable determinations. This procedure could perhaps also be useful for Thellier type palaeointensity determinations (Morales *et al.* 2001). Despite the low success rate of palaeointensity determinations, combination of three Thellier-Coe and four Tsunakawa-Shaw successful determinations yields a multimethod palaeointensity result $B = (36.9 \pm 2.0)$ μT in good agreement with the expected field intensity. The multimethod approach can be a robust reliability criterium for successful determinations.

ACKNOWLEDGMENTS

This work was funded by project PID2019-105796GB-100/AEI/10.13039/501100011033 (Spanish Agencia Estatal de Investigación), project BU037P23 (Junta de Castilla y León and the European Research and Development Fund, ERDF) and JSPS KAKENHI Grant No. 21H01171. We thank Antonio González (Cabildo de La Palma) for his invaluable support and help during our visit to the island of La Palma. We also wish to thank Dr Eugenio Fraile Nuez (IEO-CSIC) for providing us the submarine lava flow samples. We also wish two thank two anonymous reviewers for helpful comments.

SUPPORTING INFORMATION

Supplementary data are available at *GJIRAS* online.

Please note: Oxford University Press is not responsible for the content or functionality of any supporting materials supplied by the authors. Any queries (other than missing material) should be directed to the corresponding author for the paper.

DATA AVAILABILITY

Data sets for this research are available under the following reference: Calvo-Rathert, M., Vernet, E., Sánchez-Moreno, E.-M., Bógalo, M.-F. & Carrancho, Á. (2024). Rock-magnetic, palaeomagnetic and palaeointensity data from a lava flow erupted on 4 December 2021 in La Palma (Canary Islands, Spain) [Data set]. Zenodo. https://doi.org/10.5281/zenodo.12764107

REFERENCES

Alken, P. *et al.*, 2021. International Geomagnetic Reference Field: the thirteenth generation, *Earth Planets Space,* **73,** 49, doi:10.1186/s40623-020-01288-x.

Allington, M.L., Batt, C.M., Hill, M.J., Nilsson, A., Biggin, A.J. & Card, N. 2021. Obtaining archaeointensity data from British Neolithic pottery: a feasibility study, *J. Archaeol. Sci. Rep.,* **37,** 102895, doi:10.1016/j.jasrep.2021.102895.

Alonso, I., Santana-Sarmiento, F.J., Andrés-Araujo, F., Casamayor, M., Montoya-Montes, I., Brenes, A., Herrera, R. & Sánchez-García, M.J., 2023. Morphosedimentary characteristics and formation mechanisms of new beaches generated after the Tajogaite volcano eruption of 2021 (La Palma, Spain), *Mar. Geol.,* **462,** doi:10.1016/j.margeo.2023.107099.

Béguin, A., Paterson, G.A., Biggin, A.J. & de Groot, L.V. 2020. Paleointensity.org: an online, open source, application for the interpretation of paleointensity data, *Geochem. Geophys. Geosyst.,* **21,** e2019GC008791, doi:10.1029/2019GC008791.

Biggin, A. & Paterson, G., 2014. A new set of qualitative reliability criteria to aid inferences on paleomagnetic dipole moment variations through geological time, *Front. Earth. Sci.,* **2,** doi:10.3389/feart.2014.00024.

Biggin, A. & Poidras, T., 2006. First-order symmetry of weak field partial thermoremanence in multidomain ferromagnetic grains. 1. Experimental evidence and physical implications, *Earth planet. Sci. Lett.,* **245,** 438–453.

Bloemendal, J., King, J.W., Hall, F.R. & Doh, S.J., 1992. Rock magnetism of late Neogene and Pleistocene deep-sea sediments: relationship of sediment source, diagenetic processes and sediment lithology, *J. geophys. Res.,* **97,** 4361–4375.

Böhnel, H., Herrero-Bervera., E. & Dekkers, M., 2011. Paleointensities of the Hawaii 1955 and 1960 lava flows: further validation of the multispecimen method, in *The Earth's Magnetic Interior,* Vol. **1,** pp. 195–211, eds Petrovský, E., Ivers, D., Harinarayana, T. & Herrero-Bervera, E., IAGA Special Sopron Book Series, Springer.

Bowles, J.A., Jackson, M.J., Berquó, T.S., Sølheid, P.A. & Gee, J.S., 2013. Inferred time- and temperature-dependent cation ordering in natural titanomagnetites, *Nat. Commun.,* **4,** doi:10.1038/ncomms2938.

Calvo Rathert, M., Carrancho, Á., Morales, J., Pérez-Rodríguez, N., Lebedev, V.A., Caccavari, A., Vegas, N. & Goguitchaichvili, A., 2022. Multimethod palaeointensity results from a rapidly emitted upper Miocene lava flow sequence in São Vicente (Cape Verde): new data for the African record, *Geophys. J. Int.,* **231**(1), 215–229.

Calvo-Rathert, M., Bógalo, M.F., Morales, J., Goguitchaichvili, A., Lebedev, V.A., Vashakidze, G., García-Redondo, N. & Herrero-Bervera, E., 2021. An integrated paleomagnetic, multimethod-paleointensity, and radiometric study on Cretaceous and Paleogene lavas from the Lesser Caucasus: geomagnetic and tectonic implications, *J. geophys. Res.,* **126,** e2020JB020019, doi:10.1029/2020JB020019.

Calvo-Rathert, M., Morales-Contreras, J., Carrancho, Á. & Goguitchaichvili, A., 2016. A comparison of Thellier-type and multispecimen paleointensity determinations on Pleistocene and historical lava flows from Lanzarote (Canary Islands, Spain), *Geochem. Geophys. Geosyst.,* **17,** 3638–3654.

Calvo-Rathert, M., Morales, J., Carrancho, A., Camps, P., Goguitchaichvili, A. & Hill, M.J., 2019. Reproducibility of archaeointensity determinations with a multimethod approach on archaeological material reproductions, *Geophys. J. Int.,* **218,** 1719–1738.

Calvo, M., Prévot, M., Perrin, M. & Riisager, J., 2002. Investigating the reasons for the failure of paleointensity experiments: a study on historical lava flows from Mt Etna, *Geophys. J. Int.,* **149,** 44–63.

Carracedo, J.C. *et al.* 2022. The 2021 eruption of the Cumbre Vieja volcanic ridge on La Palma, Canary Islands, *Geol. Today,* **38**(3), 94–107.

Carracedo, J.C., Badiola, E.R., Guillou, H., de La Nuez, J. & Pérez Torrado, F.J. 2001. Geology and volcanology of La Palma and El Hierro, Western Canaries, *Estudios Geológicos,* **57,** 175–273.

Carracedo, J.C., Day, S., Guillou, H., Badiola, R., E., C., J., A., Torrado, P. & F., J., 1998. Hotspot volcanism close to a passive continental margin: the Canary Islands, *Geol. Mag.,* **135**(5), 591–604.

Chadima, M. & Hrouda, F., 2006. Remasoft 3.0—a user friendly paleomagnetic data browser and analyzer, *Travaux Géophysiques,* **38,** 20–21.

Coe, R., 1967. Paleointensities of the Earth's magnetic field determined from Tertiary and Quaternary rocks, *J. geophys. Res.,* **72,** 3247–3262.

Coe, R., Grommé, S. & Mankinen, E.A., 1978. Geomagnetic paleointensities from radiocarbon-dated lava flows on Hawaii and the question of the Pacific nondipol low, *J. geophys. Res.,* **83,** 1740–1756.

Cromwell, G., Tauxe, L., Staudigel, H. & Ron, H., 2015. Paleointensity estimates from historic and modern Hawaiian lava flows using glassy basalt as a primary source material, *Phys. Earth planet. Inter.,* **241,** 44–56.

Day, R., Fuller, M. & Schmidt, V.A., 1977. Hysteresis properties of titanomagnetites: Grain-size and compositional dependence, *Phys. Earth planet. Inter.,* **13,** 260–267.

De Groot, L.V. *et al.*, 2015. High paleointensities for the Canary Islands constrain the Levant geomagnetic high, *Earth planet Sci. Lett.,* **419,** 154–167.

De Groot, L.V., Biggin, A.J., Dekkers, M.J., Langereis, C.G. & Herrero-Bervera, E., 2013. Rapid regional perturbations to the recent global geomagnetic decay revealed by a new Hawaiian record, *Nat. Commun.,* **4,** 2727–2727.

Dearing, J.A., Bird, P.M., Dann, R.J.L. & Benjamin, S.F., 1997. Secondary ferrimagnetic minerals in Welsh soils: a comparison of mineral magnetic detection methods and implications for mineral formation, *Geophys. J. Int.,* **130(3),** 727–736.

Dearing, J.A., Dann, R.J.L., Hay, K., Lees, J.A., Loveland, P.J., Maher, B.A. & O'Grady, K., 1996. Frequency-dependent susceptibility measurements of environmental materials, *Geophys. J. Int.,* **124,** 228–240.

Dekkers, M.J. & Böhnel, H.N., 2006. Reliable absolute palaeointensities independent of magnetic domain state, *Earth planet. Sci. Lett.,* **284,** 508–517.

Dunlop, D., 2002. Theory and application of the Day plot (Mrs/Ms versus Hcr/Hc) 1. Theoretical curves and tests using titanomagnetite data, *J. geophys. Res.,* **107**(B3), EPM 4–1-EPM 4-22.

Dunlop, D.J., 2011. Physical basis of the Thellier-Thellier and related paleointensity methods, *Phys. Earth planet. Inter.,* **187,** 118–138.

Dunlop, D.J.y. & Özdemir, Ö., 1997. *Rock Magnetism. Fundamentals and Frontiers*. Cambridge Univ. Press, 573p.

Egli, R., 2003. Analysis of the field dependence of remanent magnetization curves. *J. Geophys. Res.,* **108,** 2081, doi:10.1029/2002JB002023.

Fabian, K. & Leonhardt, R., 2010. Multi-specimen absolute paleointensity determination: an optimal protocol including pTRM normalization, domain-state correction, and alteration test, *Earth planet. Sci. Lett.,* **297,** 84–94.

Fabian, K., 2003. Some additional parameters to estimate domain state from isothermal magnetization measurements, *Earth planet. Sci. Lett.,* **213,** 337–345.

Fukuma, K., 2023. Testing determinations of Thellier paleointensities on 1962 and 1983 lava flows and scoriae in Miyakejima, Japan, *Earth, Planets Space,* **75,** doi:10.1186/s40623-023-01781-z.

García-Redondo, N. *et al.* 2021. Further evidence of high intensity during the Levantine Iron Age Anomaly in southwestern Europe: full vector

archeomagnetic dating of an Early Iron Age dwelling from Western Spain, *J. geophys. Res.,* **126,** e2021JB022614, doi:10.1029/2021JB022614.

González, P.J., 2022. Volcano-tectonic control of Cumbre Vieja, *Science,* **375**(6587), 1348–1349.

Grappone, J.M., Biggin, A.J. & Hill, M.J., 2019. Solving the mystery of the 1960 Hawaiian lava flow: implications for estimating Earth's magnetic field, *Geophys. J. Int.,* **218,** 1796–1806.

Grommé, C.S., Wright, T.L. & Peck, D.L., 1969. Magnetic properties and oxidation of iron-titanium oxide minerals in Alae and Makaopuhi lava lakes, Hawaii, *J. geophys. Res.,* **74,** 5277–5293.

Harrison, R.J. & Feinberg, J.M., 2008. FORCinel: an improved algorithm for calculating first-order reversal curve distributions using locally weighted regression smoothing, *Geochem. Geophys. Geosyst.,* **9**(5), doi:10.1029/2008GC001987.

INFOIGME 2024. Visor cartográfico. Erupción volcánica en La Palma. Visores—Geología, evolución de la lava y terremotos. Available at: https://info.igme.es/visor/?Configuracion=Enjambre-Terremotos-La-Palma&Extension=-17.93,28.57,-17.82,28.65,4326.

Jeong, D., Liu, Q., Yamamoto, Y., Yu, Y., Zhao, X. & Qin, H., 2021. New criteria for selecting reliable Thellier–type paleointensity results from the 1960 Kilauea lava flows, Hawaii, *Earth, Planets Space,* **73,** doi:10.1186/s40623-021-01473-6.

Kitahara, Y., Yamamoto, Y., Ohno, M., Kuwahara, Y., Kameda, S. & Hatakeyama, T., 2018. Archeointensity estimates of a tenth-century kiln: first application of the Tsunakawa–Shaw paleointensity method to archeological relics, *Earth Planets Space,* **70,** doi:10.1186/s40623-018-0841-5.

Klügel, A., Galipp, K., Hoernie, K., Hauff, F. & Groom, S., 2017. Geochemical and volcanological evolution of La Palma, Canary Islands, *J. Petrol.,* **58,** 1227–1248.

Leonhardt, R., 2006. Analyzing rock magnetic measurements: the RockMagAnalyzer 1.0 software, *Comput. Geosci.,* **32,** 1420–1431.

Leonhardt, R., Heunemann, C. & Krása, D., 2004. Analyzing absolute paleointensity determinations: acceptance criteria and the software ThellierTool4.0, *Geochem. Geophys. Geosyst.,* **5**(12), doi:10.1029/2004GC000807.

Leonhardt, R., Hufenbecher, F., Heider, F. & Soffel, H., 2000. High absolute palaeointensity during a mid-Miocene excursion of the Earth's magnetic field, *Earth planet. Sci. Lett.,* **184,** 141–154.

Lied, P., Kontny, A., Nowaczyk, N. *et al.* 2020. Cooling rates of pyroclastic deposits inferred from mineral magnetic investigations: a case study from the Pleistocene Mýtina Maar (Czech Republic), *Int. J. Earth. Sci.,* **109,** 1707–1725

Lloyd, S.J., Paterson, G.A., Thallner, D. & Biggin, A.J., 2021. Improvements to the Shaw-Type Absolute Palaeointensity Method, *Front. Earth Sci.,* **9,** 701863, doi:10.3389/feart.2021.701863.

Maxbauer, D.P., Feinberg, J.M. & Fox, D.L., 2016. MAX UnMix: a web application for unmixing magnetic coercivity distributions, *Comput. Geosci.,* **95,** 140–145.

Michalk, D., Muxworthy, A.R., Böhnel, H., MacLennan, J. & Nowaczyk, N.R., 2008. Evaluation of the multispecimen parallel differential pTRM method: a test on historical lavas from Iceland and Mexico, *Geophys. J. Int.,* **173,** 409–420.

Michalk, D.M., Biggin, A.J., Knudsen, M.F., Böhnel, H.N., Nowaczyk, N., Ownby, S. & López-Martínez, M., 2010. Application of the multispecimen paleointensity method to Pleistocene lava flows from the Trans-Mexican Volcanic Belt, *Phys. Earth planet. Int.,* **179**(3-4), 139, doi:10.1016/j.pepi.2010.01.005.

Monster, M.W.L., de Groot, L.V. & Dekkers, M.J., 2015b. MSP-Tool: A VBA-Based software tool for the analysis of multispecimen paleointensity data, *Front. Earth Sci.,* **3,** 1–9.

Monster, M.W.L., de Groot, L.V., Biggin, A.J. & Dekkers, J.M., 2015a. The performance of various palaeointensity techniques as a function of rock magnetic behavior—a case study for La Palma, *Phys. Earth planet. Inter.,* **242,** 36–49.

Morales, J., Gogutchaichvili, A., Alva-Valdivia, L. & Soler, A.M., 2001. Low-temperature demagnetization of volcanic rocks containing multidomain magnetic grains: Implications for the Thellier paleointensity determinations, *Geof. Int.,* **40**(4), 293–300.

Néel, L. 1949. Théorie du traînage magnétique des ferromagnétiques en grains fins avec applications aux terres cuites, *Annales de Géophysique,* **5,** 99–136.

Palanco, S. *et al.* 2022. Field deployment of a man-portable stand-off laser-induced breakdown spectrometer: a preliminary report on the expedition to the Cumbre Vieja volcano (La Palma, Spain, 2021), *Spectrochim. Acta B At. Spectrosc.,* **190,** doi:10.1016/j.sab.2022.106391.

Parés, J.M., Vernet, E., Calvo-Rathert, Soler, V., Bógalo, M.F. & Álvaro, A., 2022. Rock Magnetism of Lapilli and Lava Flows from Cumbre Vieja Volcano, 2021 Eruption (La Palma, Canary Islands): initial reports, *Geosciences,* **12**(7), doi:10.3390/geosciences12070271.

Paterson, G.A., Tauxe, L., Biggin, A.J., Shaar, R. & Jonestrask, L.C. 2014. On improving the selection of Thellier-type paleointensity data, *Geochem. Geophys. Geosyst.,***15,** 1180–1192.

Petrovský, E. & Kapička, A., 2006. On determination of the Curie point from thermomagnetic curves, *J. geophys. Res.,* **111**(B12), doi:10.1029/2006JB004507.

Pick, T. & Tauxe, L., 1994. Characteristics of magnetite in submarine basaltic glass, *Geophys. J. Int.,* **119,** 116–128.

Pike, C., Roberts, A.P. & Verosub, K.L. 1999. Characterising interactions in fine magnetic particle system using first order reversal curves, *J. appl. Phys.,* **85,** 6660–6667.

Prévot, M., 1981. Some aspects of magnetic viscosity in subaerial and submarine volcanic rocks, *Geophys. J. R. astr. Soc.,* **66,** 169–192.

Riisager, J., Perrin, M., Riisager, P. & Ruffet, G., 2000. Paleomagnetism, paleointensity, and geochronology of Miocene basalts and baked sediments from Velay Oriental, *J. geophys. Res.,* **105,** 883–896.

Roberts, A.P., Pike, C.R. & Verosub, K.L., 2000. First-order reversal curves diagrams: a new tool for characterizing the magnetic properties of natural samples, *J. geophys. Res.,* **105,** 28 461–28 475.

Roberts, A.P., Tauxe, L., Heslop, D., Zhao, X. & Jiang, Z.X., 2018. A critical appraisal of the "Day Diagram", *J. geophys. Res.,* **123**(4), 2618–2644.

Rolph, T.C. & Shaw, J., 1985. A new method of palaeofield magnitude correction for thermally altered samples and its application to Lower Carboniferous lavas, *Geophys. J. Int.,* **80,** 773–781.

Sánchez-Moreno, E.M., Calvo-Rathert, M., Goguitchaichvili, A., Vashakidze, G.T., Camps, P., Morales-Contreras, J., Vegas-Tubía, N. & Lebedev, V.A. 2021. Paleointensity results from Pliocene lavas of the Lesser Caucasus obtained using the multispecimen parallel differential pTRM method: a comparison with Thellier-Thellier and IZZI data, *J. geophys. Res.,* **126,** e2020JB019682, doi:10.1029/2020JB019682.

Shaw, J., 1974. A new method of determining the magnitude of the paleomagnetic field. Application to five historic lavas and five archaeological samples, *Geophys. J. R. astr. Soc.,* **39,** 133–141.

Shcherbakov, V.P., Gribov, S.K., Lhuillier, F., Aphinogenova, N.A. & Tsel'movich, V.A., 2019. On the reliability of absolute paleointensity determinations on basaltic rocks bearing a thermochemical remanence, *J. geophys. Res.,* **124,** 7616–7632.

Spassov, S., Heller, F., Kretzschmar, R., Evans, M.E., Yue, L.P. & Nourgaliev, D.K., 2003. Detrital and pedogenic magnetic mineral phases in the loess/palaeosol sequence at Lingtai (Central Chinese Loess Plateau), *Phys. Earth planet. Inter.,* **140,** 255–275.

Tauxe, L. *et al.* 2016. PmagPy: software package for paleomagnetic data analysis and a bridge to the Magnetics Information Consortium (MagIC) Database, *Geochem., Geophys. Geosyst.,* **17,** 2450–2463.

Tauxe., L., Mullender, T.A.T. & Pick, T., 1996. Potbellies, wasp-waists, and superparamagnetism in magnetic hysteresis, *J. geophys. Res.,* **101**(B1), 571–583.

Thellier, E. & Thellier, O. 1959. Sur l'intensité du champ magnétique terrestre dans le passé historique et géologique, *Ann. Geophys.,* **15,** 285–376.

Thellier, E. & Thellier, O., 1944. Recherches géomagnétiques sur des coulées volcaniques d'Auvergne, *Ann. Geophys.,* **1,** 37–52

Tsunakawa, H. & Shaw, J. 1994. The Shaw method of paleointensity determinations and its application to recent volcanic rocks, *Geophys. J. Int.,* **118,** 781–787

Tsunakawa, H., Shimura, K. & Yamamoto, Y., 1997. Application of double heating technique of the Shaw method to the Brunhes epoch volcanic rocks

(abstract), in *Proceedings of the 8th Scientific Assembly IAGA, Abstract Book,* August 1997, Uppsala, Vol. **85,** IAGA.

Valet, J.P., Herrero-Bervera, E., Carlut, J. & Kondopoulou, D., 2010. A selective procedure for absolute paleointensity in lava flows, *Geophys. Res. Lett.,* **37**(16), doi:10.1029/2010GL044100.

Yamamoto, Y. & Tsunakawa, H. 2005. Geomagnetic field intensity during the last 5 Myr: LTD-DHT Shaw palaeointensities from volcanic rocks of the Society Islands, French Polynesia, *Geophys. J. Int.,* **162,** 79–114.

Yamamoto, Y., Tauxe, L., Ahn, H.-S. & Santos, C. 2022. Absolute paleointensity experiments on aged thermoremanent magnetization: assessment of reliability of the Tsunakawa-Shaw and other methods with Implications for "fragile" curvature, *Geochem. Geophys. Geosyst.,* **23**(4), doi:10.1029/2022GC010391.

Yamamoto, Y., Tsunakawa, H. & Shibuya, H. 2003. Paleointensity study of the Hawaiian 1960 lava: implications for possible causes of erroneously high intensities, *Geophys. J. Int.,* **153,** 263–276.